doi:10.1093/plphys/kiab299 PLANT PHYSIOLOGY 2021: 187: 1462–1480

Plant Physiology®

Research Article

Optical topometry and machine learning to rapidly phenotype stomatal patterning traits for maize QTL mapping

Jiayang Xie [1,2], Samuel B. Fernandes [1,3], Dustin Mayfield-Jones [2,3,4], Gorka Erice [2,†], Min Choi,[2] Alexander E. Lipka [1,3] and Andrew D.B. Leakey [1,2,3,4,*,‡]

1 Department of Crop Sciences, University of Illinois at Urbana-Champaign, Urbana, Illinois 61801, USA
2 Carl R. Woese Institute for Genomic Biology, University of Illinois at Urbana-Champaign, Urbana, Illinois 61801, USA
3 Center for Digital Agriculture, University of Illinois at Urbana-Champaign, Urbana, Illinois 61801, USA
4 Department of Plant Biology, University of Illinois at Urbana-Champaign, Urbana, Illinois 61801, USA

*Author for communication: leakey@illinois.edu
†Present address: Agrotecnologías Naturales S.L., 43762 Tarragona, Spain.
‡Senior author.

A.D.B.L. and J.X. conceived and designed the original research plans; J.X. performed the experiments; G.E. developed the data collection methods and performed preliminary genotype screening; M.C. provided the technical assistance; J.X. and D.M-J. conceived and developed the machine learning pipeline; J.X., S.B.F., A.E.L., and A.D.B.L. analyzed the data; J.X., D.M.-J., S.B.F., A.E.L., and A.D.B.L. wrote the article with contributions from all of the authors; A.D.B.L. agrees to serve as the author responsible for contact and ensures communication.
The author responsible for distribution of materials integral to the findings presented in this article in accordance with the policy described in the Instructions for Authors (https://academic.oup.com/plphys/pages/general-instructions) is: Andrew D.B. Leakey (leakey@illinois.edu).

Abstract

Stomata are adjustable pores on leaf surfaces that regulate the tradeoff of CO_2 uptake with water vapor loss, thus having critical roles in controlling photosynthetic carbon gain and plant water use. The lack of easy, rapid methods for phenotyping epidermal cell traits have limited discoveries about the genetic basis of stomatal patterning. A high-throughput epidermal cell phenotyping pipeline is presented here and used for quantitative trait loci (QTL) mapping in field-grown maize (*Zea mays*). The locations and sizes of stomatal complexes and pavement cells on images acquired by an optical topometer from mature leaves were automatically determined. Computer estimated stomatal complex density (SCD; $R^2 = 0.97$) and stomatal complex area (SCA; $R^2 = 0.71$) were strongly correlated with human measurements. Leaf gas exchange traits were genetically correlated with the dimensions and proportions of stomatal complexes ($r_g = 0.39–0.71$) but did not correlate with SCD. Heritability of epidermal traits was moderate to high ($h^2 = 0.42–0.82$) across two field seasons. Thirty-six QTL were consistently identified for a given trait in both years. Twenty-four clusters of overlapping QTL for multiple traits were identified, with univariate versus multivariate single marker analysis providing evidence consistent with pleiotropy in multiple cases. Putative orthologs of genes known to regulate stomatal patterning in Arabidopsis (*Arabidopsis thaliana*) were located within some, but not all, of these regions. This study demonstrates how discovery of the genetic basis for stomatal patterning can be accelerated in maize, a C_4 model species where these processes are poorly understood.

Received October 09, 2020. Accepted May 26, 2021. Advance access publication July 9, 2021

Introduction

Stomata are the adjustable pores on leaf surfaces that regulate gas exchange, most notably CO_2 uptake and water vapor loss. The ratio of carbon gained to water lost is defined as water use efficiency (WUE), and represents arguably the most fundamental tradeoff faced by land plants (Leakey et al., 2019). At the leaf level, this is most commonly expressed as intrinsic WUE (*iWUE*), which is calculated as the ratio of the net rate of CO_2 assimilation (A) to stomatal conductance (g_s). The pattern of stomata on the epidermis, and the dynamics of stomatal opening and closing, influence many important processes from food and energy production to global carbon and water cycling (Hetherington and Woodward, 2003). The accessibility of stomata on the plant exterior surface has also made them a model system for studying developmental and signaling processes (Blatt, 2000; Schroeder et al., 2001; Bergmann, 2004; Lawson et al., 2014; Torii, 2015). Consequently, there is a significant potential for fundamental scientific discoveries about stomata to be leveraged for improvement of crop performance and sustainability through breeding or biotechnology (Yoo et al., 2010; Franks et al., 2015; Hughes et al., 2017; Caine et al., 2019; Lawson and Vialet-Chabrand, 2019; Harrison et al., 2020; McKown and Bergmann, 2020).

Despite the accessibility and importance of stomata, assessing the patterning of epidermal cells has remained a laborious and time-consuming task for many decades. Most studies of stomatal patterning still rely on methods of imprinting or peeling the epidermis from live tissue, followed by light microscopy, and manual identification and measurement of cells in images (e.g., Biscoe, 1872; Caine et al., 2019; Vőfély et al., 2019). This limits the application of quantitative, forward, and reverse genetics to understand the genes, and processes that regulate stomatal patterning. And, it means samples cannot be analyzed with sufficient throughput for stomatal patterning to be a target trait in modern crop breeding programs.

Optical topometry (OT) is a rare example of a methodology proposed to accelerate the acquisition of epidermal patterning data through rapid image acquisition. OT is a nondestructive method for use on fresh or frozen leaf samples, which requires no sample preparation beyond sticking a piece of leaf to a microscope slide with double-sided sticky tape (Haus et al., 2015). It gathers focused pixels across plains of the leaf surface in <1 min per field of view. OT images have been manually counted to assess stomatal density responses to elevated [CO_2] in Arabidopsis (*Arabidopsis thaliana*; Haus et al., 2018). But an automated analysis pipeline is still needed to robustly capture within-species genetic variation in epidermal patterning from OT images with the fidelity required for genetic analysis.

There have been many attempts to address the phenotyping bottleneck for stomatal patterning through computer-aided image analysis. Classical image processing methods (Omasa and Onoe, 1984; Liu et al., 2016; Duarte et al., 2017) and machine learning models have been applied (Vialet-Chabrand and Brendel, 2014; Higaki et al., 2015; Jayakody et al., 2017; Saponaro et al., 2017; Dittberner et al., 2018; Toda et al., 2018; Aono et al., 2019; Bhugra et al., 2019; Fetter et al., 2019; Li et al., 2019; Sakoda et al., 2019). Although a number of these methods have been demonstrated to work within constrained image sets, none of them have been widely adopted, even within a single species. Some of these tools require scanning electron microscopy, adding to the sample preparation and image acquisition burden (Aono et al., 2019; Bhugra et al., 2019; Fetter et al., 2019). Most existing tools are limited to identifying and phenotyping stomatal complexes. Adding the ability to measure pavement cells is valuable in its own right and also allows calculation of stomatal index (SI; i.e., the ratio of stomata number to total epidermal cell number given in unit leaf area). SI is a key trait because it is directly influenced by mechanisms that regulate epidermal cell fate and is less sensitive to environmental influences than stomatal density (Royer, 2001). Therefore, developing an end-to-end pipeline for rapid acquisition and comprehensive analysis of epidermal cell patterning, and demonstrating its application in the investigation of genetic variation in stomatal patterning, remain an important but elusive goal.

In recent years, important progress has been made in studying the degree to which orthologs of stomatal patterning genes in Arabidopsis (Pillitteri and Torii, 2012) have conserved or novel functions in C_3 grass species (Raissig et al., 2016; Hughes et al., 2017; Raissig et al., 2017; Yin et al., 2017; Hepworth et al., 2018; McKown and Bergmann, 2020). But, very little is known about the trait relationships and genetic control of stomatal patterning and *iWUE* in C_4 species (Leakey et al., 2019). And, apart from a few notable examples (Cartwright et al., 2009; Campitelli et al., 2016; Raissig et al., 2017), quantitative genetics and forward genetic screens to identify putative regulators of stomatal patterning still have generally not met their potential to drive discovery of genotype-to-phenotype relationships.

Linkage mapping in barley (*Hordeum vulgare*), wheat (*Triticum aestivum*), and rice (*Oryza sativa*) has discovered quantitative trait loci (QTL) that are associated with stomatal patterning traits (Patto et al., 2003; Laza et al., 2010; Liu et al., 2014, 2017; Sumathi et al., 2018), including some that colocalize with yield QTL (Shahinnia et al., 2016). But, the only reports of similar experiments in maize predate statistical techniques, such as QTL mapping (Heichel, 1971). Maize is the most important crop in the world in terms of total production (USDA, 2019), with the Midwest USA producing ~27% of the global harvest (USDA-FAS, 2020). Maize yield is limited by water availability, and increasingly sensitive to drought as a side effect of productivity increases resulting from improved breeding and management (Lobell et al., 2014). Conversely, increased maize production over recent decades has led to faster water cycling and regional cooling in Midwest USA (Alter et al., 2018). Therefore, improved understanding of the genetic basis for variation in stomatal traits in maize has implications for agricultural productivity,

resilience, and sustainability. Fortunately, maize is also a highly tractable, model experimental system for crop genetics (Buckler et al., 2009).

In summary, the current study was motivated by the need for a tool to accelerate phenotyping of epidermal cell patterning, which could then be demonstrated by applying it to investigate the genetic architecture and trait relationships of stomatal patterning traits in maize. The desired characteristics of an end-to-end phenotyping pipeline are: (1) little to no sample preparation and quick image acquisition; (2) fast, accurate, and robust detection of epidermal cells; and (3) the ability to extract the number, size, and position of pavement cells as well as stomatal complexes. OT was tested as a data acquisition method from leaves that were stored frozen after being grown in the field. For epidermal cell detection, the recently developed Mask R-CNN model for object instance detection (He et al., 2017) was tested to treat stomata and pavement cells as two object classes, so that their position and size could be extracted simultaneously. A recombinant inbred line (RIL) population resulting from a B73 × MS71 cross was grown in 2 years in the field. Stomatal patterning was phenotyped along with leaf photosynthetic gas exchange and specific leaf area (SLA) to investigate trait relationships and their genetic architecture in a major crop and model C_4 species.

Results

High-throughput phenotyping pipeline for epidermal cells of maize

A high-throughput epidermal cell detection pipeline requires both efficient image acquisition and automatic cell detection (Figure 1). OT allowed rapid, nondestructive imaging of leaf samples. Less than 1 min was required from locating the portion of the epidermis to be scanned to outputting a 3D topography surface layer with dimensions of 0.8 mm × 0.8 mm (e.g., Figure 2A). Overall, 7,033 fields of view were sampled from 1,569 leaf samples collected over two field seasons, with scanning completed in approximately 24 person-days. The Mask Region Based Convolutional Neural Network (R-CNN) model automatically detected stomatal complexes as well as pavement cells, even though the latter varied greatly in their physical shape and size (Figure 2; Supplemental Figure S1). Image pre-processing and analysis of a full image set for QTL mapping (~4,000 images) was completed in ~120 h (Table 1). Anatomical trait names with corresponding acronyms, descriptions, and units are listed in Table 2.

Human validation of Mask R-CNN cell counts and stomatal complex size

A comparison was drawn between the machine and six trained human evaluators, each labeling a full set of images, to verify the machine's performance on epidermal cell recognition and boundary predictions. Variation among human evaluators contributed a small portion of the variance within the dataset for both SCD (2%) and pavement cell density (PD; 6%; Supplemental Figure S2). Variation among evaluators contributed a greater proportion of variance for stomatal complex width (SCW; 56%), stomatal complex length (SCL, 23%), and stomatal complex area (SCA; 15%). Nonetheless, uncertainty around the mean value of human measurements was low (expressed as standard error around plotted data in Figures 3, A and B, 4). There was no variance in estimates of cell density from Mask R-CNN when the same image was repeatedly submitted to the analysis pipeline, so no measure of technical variation could be expressed.

The mean density of cells estimated by the group of human evaluators was very strongly correlated with computer estimation of both SCD ($R^2 = 0.97$, $P < 0.0001$; Figure 3A) and PD ($R^2 = 0.96$, $P < 0.0001$; Figure 3B) and displayed very low bias from the 1:1 line. The mean data from human evaluators were also highly significantly correlated with computer measurements for SCL ($R^2 = 0.81$, $P < 0.0001$; Figure 4A), SCW ($R^2 = 0.54$, $P < 0.0001$; Figure 4B) and SCA ($R^2 = 0.71$, $P < 0.0001$; Figure 4C). All three traits were slightly underestimated by machine measurements relative to human measurements, with the absolute bias being greater for larger cells than small cells.

To further evaluate sources of variation in stomatal patterning traits, six RILs were chosen that represented the range of SCD observed across the full mapping population in the 2016 growing season. All the images for those six RILs were then manually counted by five human beings as well as by machine. Variation around the genotype means derived from machine counts was similar or smaller than the variation resulting from using the mean of five expert evaluators as the input (expressed as standard error around plotted data in Figure 3, C and D). Genotype mean values based on machine counts were very strongly correlated with best-estimates from human evaluators for both stomatal complex density (SCD; $R^2 = 0.999$, $P < 0.0001$; Figure 3C) and PD ($R^2 = 0.998$, $P < 0.0001$; Figure 3D), and had very little bias from the 1:1 line.

Heritability and trait variation across the RIL population

Genotypic variation in stomatal patterning traits displayed good repeatability across growing seasons (Figure 5). Genotype means were significantly correlated across the 2 years for all traits assessed with goodness-of-fit (R^2) ranked from highest to lowest of: 0.70 for stomatal complex total area (SCTA); 0.69 for stomatal pore area index (SPI), 0.68 for SI, 0.64 for SCD; 0.64 for pavement cell area (PA); 0.60 for PD; 0.56 for SCL; 0.52 for stomatal complex length and width ratio (SCLWR); 0.50 for SCA; 0.46 for SCW; 0.43 for pavement cell total area (PTA); and 0.13 for SLA. This corresponded to all epidermal patterning traits having moderate to high heritability ($h^2 = 0.42$ to 0.82) across the 2 years (Supplemental Table S1).

Among the 191 RILs assessed over the 2 years, the relative range of stomatal patterning traits varied from more than 2-

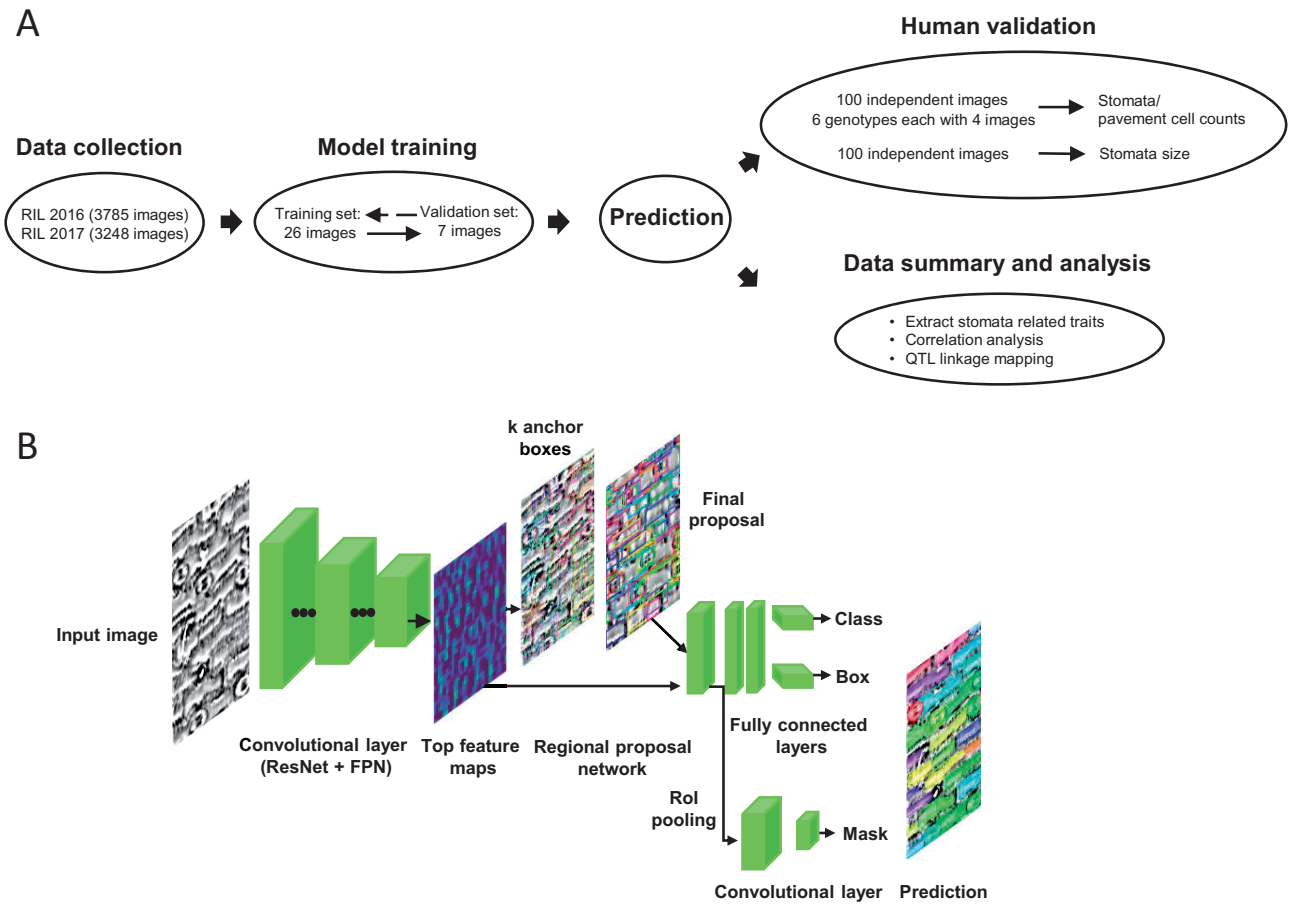

Figure 1 Overall workflow for imaging pipeline and image analysis by Mask R-CNN. Workflow of data collection, model training, model prediction, human validation, and experimental data analysis used to phenotype epidermal cell patterning traits (A). Summary of Mask R-CNN approach to analyze images captured by OT for stomata and pavement cell detection (B). Image example was truncated from standard image.

fold, that is, 127% for SCD (59–134 mm^{-2}) down to 29% for SCW (18.8–24.3 µm; Supplemental Figure S3). SLA was significantly greater in 2017 (205–299 $cm^2\ g^{-1}$) compared with 2016 (139–220 $cm^2\ g^{-1}$). In 2017, leaf photosynthetic gas exchange traits varied 2- to 4-fold among the 192 RILs for the rate of net CO_2 assimilation (A), stomatal conductance (g_s); the ratio of intercellular [CO_2] to atmospheric [CO_2] (c_i/c_a); and *iWUE*. Consistent with there being transgressive segregation, the ranges of all trait values significantly exceeded the trait variation between the parent lines B73 and MS71 (Supplemental Figure S3). As expected, SCD and SI were significantly lower in MS71 than B73. This corresponded with greater stomatal complex size in MS71 compared to B73 in terms of SCW, SCL, and SCA. SCLWR was greater in MS71 than B73. In terms of leaf gas exchange, MS71 had lower g_s, lower A, lower c_i/c_a and greater *iWUE* than B73 (Supplemental Figure S3).

Phenotypic and genetic correlations among traits

Correlation matrices for stomatal patterning traits were very similar for data collected in 2016 (Supplemental Figure S4, A and B) and 2017 (Figure 6; Supplemental Figure S5) regardless of whether they were phenotypic or genetic correlations. Within each year, the patterns of associations among traits were also very similar in terms of genetic correlations compared to phenotypic correlations (Figure 6; Supplemental Figure S5). But, genetic correlations—which parse out environmental variance—more clearly resolved structure–function relationships. Therefore, we focus here on genetic correlations from 2017, when anatomical traits were assessed alongside leaf photosynthetic gas exchange.

Examining structure–function relationships across trait categories, A, g_s, c_i/c_a, and *iWUE* were not significantly genetically correlated with SCD (Figure 6). However, g_s was positively genetically correlated with SCW ($r_g = 0.43$) and negatively genetically correlated with SCL ($r_g = -0.44$), SCLWR ($r_g = -0.60$) and SPI ($r_g = -0.55$). *iWUE* was negatively genetically correlated with SCW ($r_g = -0.40$) and positively genetically correlated with SCLWR ($r_g = 0.54$) and SPI ($r_g = 0.59$). As a result of strong associations among the leaf gas exchange traits (e.g., Supplemental Figure S6), A had the same pattern of relationships with stomatal patterning traits as g_s. And, c_i/c_a had the same pattern of relationships with stomatal patterning traits as *iWUE*, but in the opposite direction. SLA was positively genetically correlated with *iWUE* ($r_g = 0.41$), SCD ($r_g = 0.32$), and SPI ($r_g = 0.41$). The tight

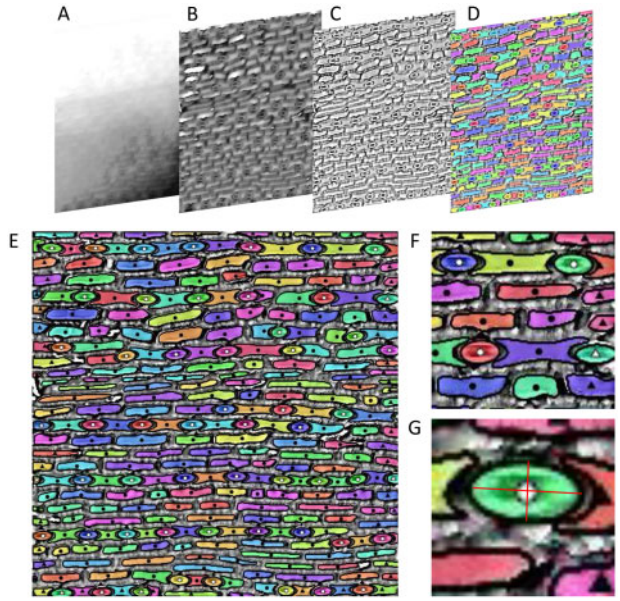

Figure 2 Example steps in the process of analyzing an OT image for epidermal cell patterning. 3D topography image layer extracted from raw filers output by the optical topometer (A), flattening by use of Robust Gaussian filters (B), contrast enhancement by use of a Laplacian filter (C), prediction of cell instances by Mask R-CNN (D–G). Cell-related traits were calculated and extracted based on cell boundary coordinates, with boundary and centroid labeled for better visualization (E). Zooming in shows stomata were labeled with white centroids while pavement cells were labeled with black centroids (F). Cells that were cut off on image edges were tagged with triangles and were excluded in estimation of average cell size. Ellipses were fit to stomatal complexes, with width and length calculated as the lengths of minor and major axis of the ellipse (red lines; G).

relationship between c_i/c_a and *iWUE* was expected since these two traits are closely mathematically related. However, genotype-to-phenotype results for the two traits included unique features. So, to avoid excluding potentially valuable information they were both retained in subsequent analysis.

There were numerous significant genetic correlations among anatomical stomatal patterning traits (Figure 6). Genotypes with larger stomatal complexes tended to have larger pavement cells (SCA vs. PA, $r_g = 0.36$), which resulted in a positive genetic correlation between SCD and PD as well ($r_g = 0.66$). SCD was negatively genetically correlated with measures of stomatal complex size, including SCL ($r_g = -0.48$) and SCA ($r_g = -0.52$). With the majority of the epidermis occupied by pavement cells, the tradeoff between density (PD) and size (PA) was even stronger than for stomatal complexes ($r_g = -0.91$). After aggregating across the epidermis, SCTA was positively genetically correlated with SCD ($r_g = 0.84$) and SI ($r_g = 0.78$) but was not genetically correlated with measures of stomatal complex size. Considering just cell identity, SI was genetically correlated with variation in SCD ($r_g = 0.72$) but not with PD.

QTL analysis

In total, 140 individual QTL were identified (Figure 7; Supplemental Table S2; Supplemental Figure S7) for the 12 traits tested in 2016 (63 QTL) and the 16 traits tested in 2017 (77 QTL). More than half of these QTL were independently identified for the same trait in both years, providing greater confidence in associations at 36 loci spread across every chromosome except chromosome 4. The percentage of phenotypic variance explained (PVE) by

Table 1 Time investment approximations for epidermal cell detection and trait extractions comparing manual measurements versus automated detections

Trait	Manual Measurement for Each Image	Manual Measurement for Mapping Population with 200 Lines	Automated Phenotyping for Mapping Population with 200 Lines
SCD	2 min	133 h	120 h*
SCA	1 h	4,000 h	
PD	8 min	533 h	
PA	3 h	12,000 h	

Estimations were done on 20X magnification maize abaxial images (0.8 mm × 0.8 mm) for a mapping population with 200 lines, four replications, and five leaf-level subsamples (4,000 images).
*Time estimation for all traits combined.

Table 2 List of extracted leaf epidermal anatomical traits and their abbreviation, description, and unit

Trait	Acronyms	Description	Unit
Stomatal Complex Density	SCD	Number of stomata in unit area	mm^{-2}
Stomatal Complex Width	SCW	Width of stomatal complex	μm
Stomatal Complex Length	SCL	Length of stomatal complex	μm
Stomatal Complex Area	SCA	Area of individual stomatal complex	$μm^2$
Stomatal Complex Total Area	SCTA	Sum of SCA in each standard image (800 × 800 $μm^2$)	$1 \times 10^3 μm^2$
Stomatal Complex Length and Width Ratio	SCLWR	SCL divided by SCW	
Pavement Cell Density	PD	Number of pavement cells in unit area	mm^{-2}
Pavement Cell Area	PA	Area of individual pavement cell	$μm^2$
Pavement Cell Total Area	PTA	Sum of PA in each standard image (800 × 800 $μm^2$)	$1 \times 10^3 μm^2$
Stomatal Index	SI	Number of stomata divided by the sum of stomata and pavement cells	%
Stomatal Pore Area Index	SPI	Stomata number multiplied by SCL squared in unit area	10^{-2}

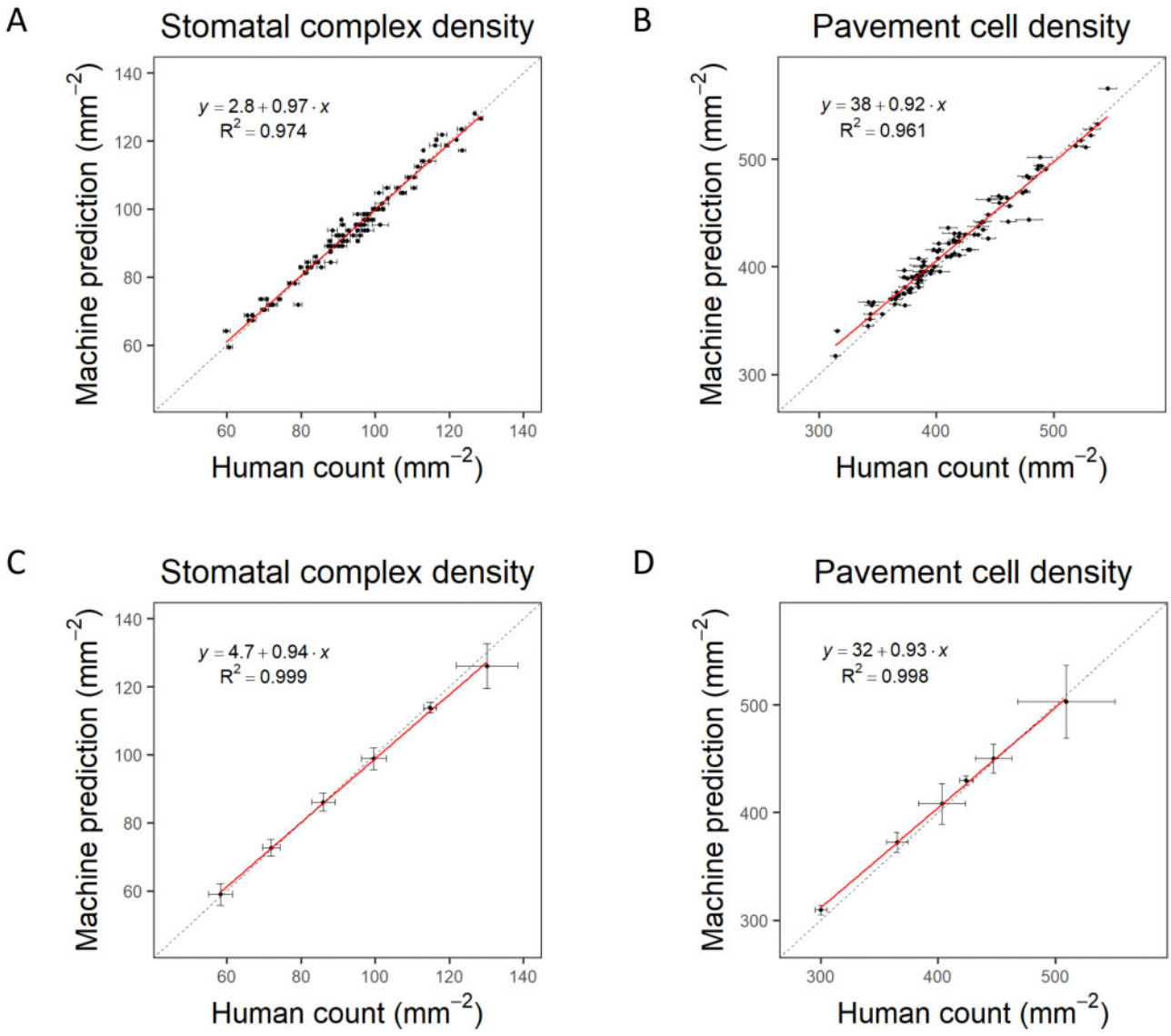

Figure 3 Scatterplots of stomatal patterning traits comparing data measured by humans versus data measured by the computer using Mask R-CNN. SCD (A and C) and PD (B and D). Plotted data describe 100 randomly selected OT images from the B73 × MS71 maize RIL population with error bars showing the standard error of technical variation among six expert human evaluators on each individual image (A and B) or genotype means for 6 RILs selected to represent the range of observed trait values in the population with error bars showing the standard error of biological variation among replicates based on the mean of predictions from five expert human evaluators or computer predictions using Mask R-CNN (C and D). There is no variance among predictions by Mask R-CNN when it is presented with a given image multiple times. The line of best fit (red line) and 1:1 line (black dashed line) are shown along with the coefficient of determination (R^2).

individual QTL was 8.7% on average, with a maximum of 19.3% for c_i/c_a at 95 centiMorgan (cM) on chromosome 1 (Figure 7; Supplemental Table S2). For the anatomical stomatal patterning traits tested in both years, the number of QTL identified varied from 5 QTL for SCL and 6 QTL for SPI to 16 QTL for SCD and 17 QTL for SI (Figure 7; Supplemental Table S2). In comparison, one to four QTL were identified for each of the functional leaf photosynthetic gas exchange traits, which were only tested in 2017. Correspondingly, the total PVE by all the QTL for a given trait was greater for the anatomical stomatal patterning traits (50.8% on average in 2017) than for the photosynthetic gas exchange traits (26.3% on average in 2017; Supplemental Figure S8). In addition, for the anatomical stomatal patterning traits, the total PVE was generally equivalent or greater in 2017 (50.8% on average) than in 2016 (46.3% on average, Supplemental Figure S8). The traits with the greatest total PVE (i.e., > 50%) were SCA, SCD, SI, SCTA, SCW, and PA. Pairwise epistatic interactions between QTL were found for SCW and SI in year 2016, as well as for SCD, SCA, g_s, and c_i/c_a in 2017 (Supplemental Table S3). But no epistatic interactions were observed consistently across years and the PVE explained by the interactions (1%–7%) was less than the average PVE observed for individual, additive QTL (Supplemental Table S2).

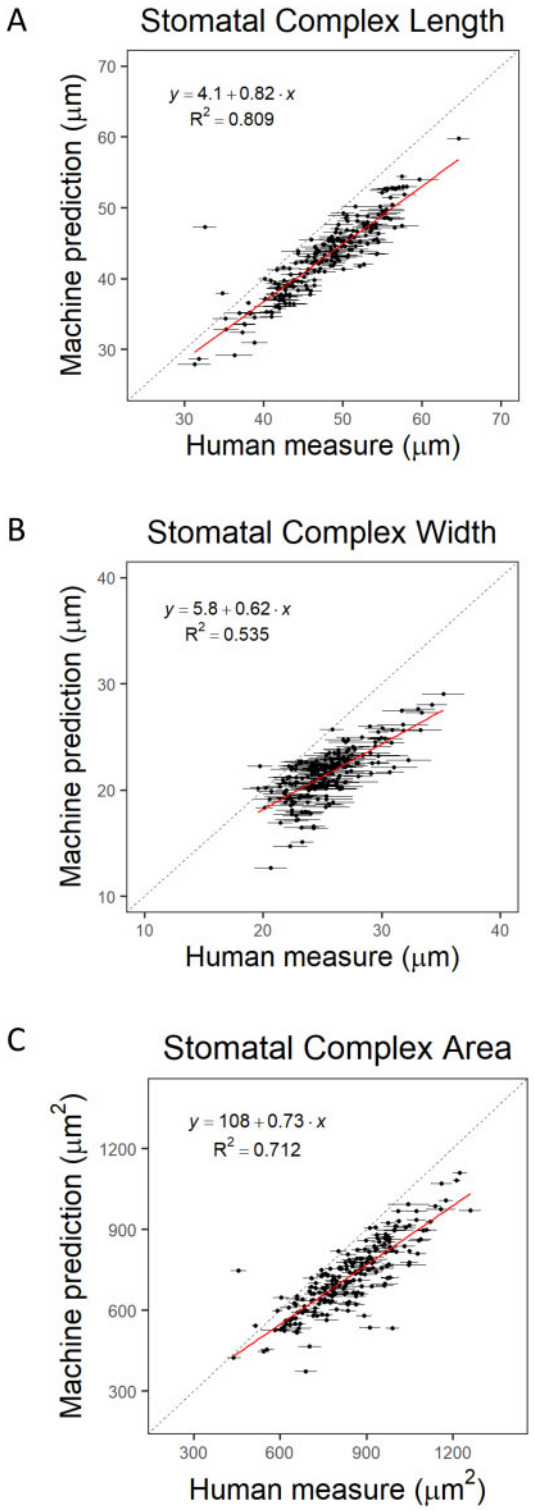

Figure 4 Scatterplots of stomatal complex size traits comparing data measured by humans versus data measured by the computer using Mask R-CNN. SCL (A); SCW (B); SCA (C). Plotted data describe 210 stomatal complexes (5 each from 42 images) randomly selected from the B73 × MS71 maize RIL population with error bars showing the standard error of technical variation among six expert human evaluators on each individual image. There is no variance among predictions by Mask R-CNN when it is presented with a given image multiple times. The line of best fit (red line) and 1:1 line (black dashed line) are shown along with the coefficient of determination (R^2).

Many of the QTL for both anatomical and functional traits were located in clusters. Overall, 24 clusters were identified and named in sequence order (Figure 7; Supplemental Table S2; e.g., Chr1A–Chr1D for clusters on chromosome 1 based on their genetic position). The number of QTL in a cluster varied from 2 (Chr1A, Chr4A, Chr6A) to 12 (Chr6D). There were many examples of QTL colocalizing for traits that are closely related (e.g., SCL, SCLWR, and SCA in cluster Chr2A or SCD, SCTA, SI, and SPI in cluster Chr9D). Interestingly, only two clusters were limited to QTL from a single category of traits. Cluster Chr1A and Chr4A contained QTL only for stomatal size traits and cluster Chr9C contained QTL only for pavement cell traits. The other 22 QTL clusters span at least two trait categories (Figure 7; Supplemental Table S2). The clusters Chr1C, Chr6B, Chr10A, and Chr10B are notable for including overlapping QTL for both epidermal anatomy traits and photosynthetic gas exchange traits.

When QTL was independently identified for the same trait in both years, the direction of the allelic effect was always consistent (Figure 7; Supplemental Table S2). Allelic effects were also generally consistent with the trait correlations previously reported. As examples, all allelic effects for QTL at a given locus had opposing directions for SCD versus SCA or PA versus PD. However, the direction of allelic effects at any individual locus was generally, but not universally, predictable from the trait means of the parental lines. For example, the MS71 allele resulted in lower SCD at 9 of the 13 loci where QTL for SCD were identified, as would be consistent with the lower trait mean for the MS71 inbred line versus B73 (Figure 7; Supplemental Table S2). And, the MS71 allele resulted in greater SCA at 7 of the 12 loci where QTL for SCA were identified, as would be consistent with the greater trait mean for the MS71 inbred line versus B73. Consistent with trait values for the parental lines, all of the statistically significant MS71 alleles resulted in lower g_s relative to B73 alleles. In contrast to other QTL, MS71 alleles in cluster Chr1C were associated with lower g_s and greater SD, highlighting the complexity of genetic control of these traits.

A total of 81 single nucleotide polymorphisms (SNPs) were identified in a follow-up test for pleiotropic causal mutations underlying the statistical associations initially identified as QTL clusters, that is, putatively pleiotropic quantitative trait nucleotides (QTNs). This involved a series of univariate and multivariate single marker analyses (Supplemental Table S4). In many cases, there was an evidence consistent with pleiotropy for different stomatal patterning traits. Three regions were highlighted as having potential to be pleiotropic for stomatal patterning and gas exchange traits. Seven QTNs at 83-96 cM on chromosome 1 fall within the Chr1C cluster and were significant for c_i/c_a and SCTA and SLA, with four of those QTNs also being significant for SCD (Supplemental Table S4). Of those seven QTNs, S_181051496 stands out as being significant for SCD, PD, SCTA, PA, SPI, SLA, g_s, and c_i/c_a. The S_15690240 QTN at 32 cM on chromosome 10 falls within the Chr10A cluster

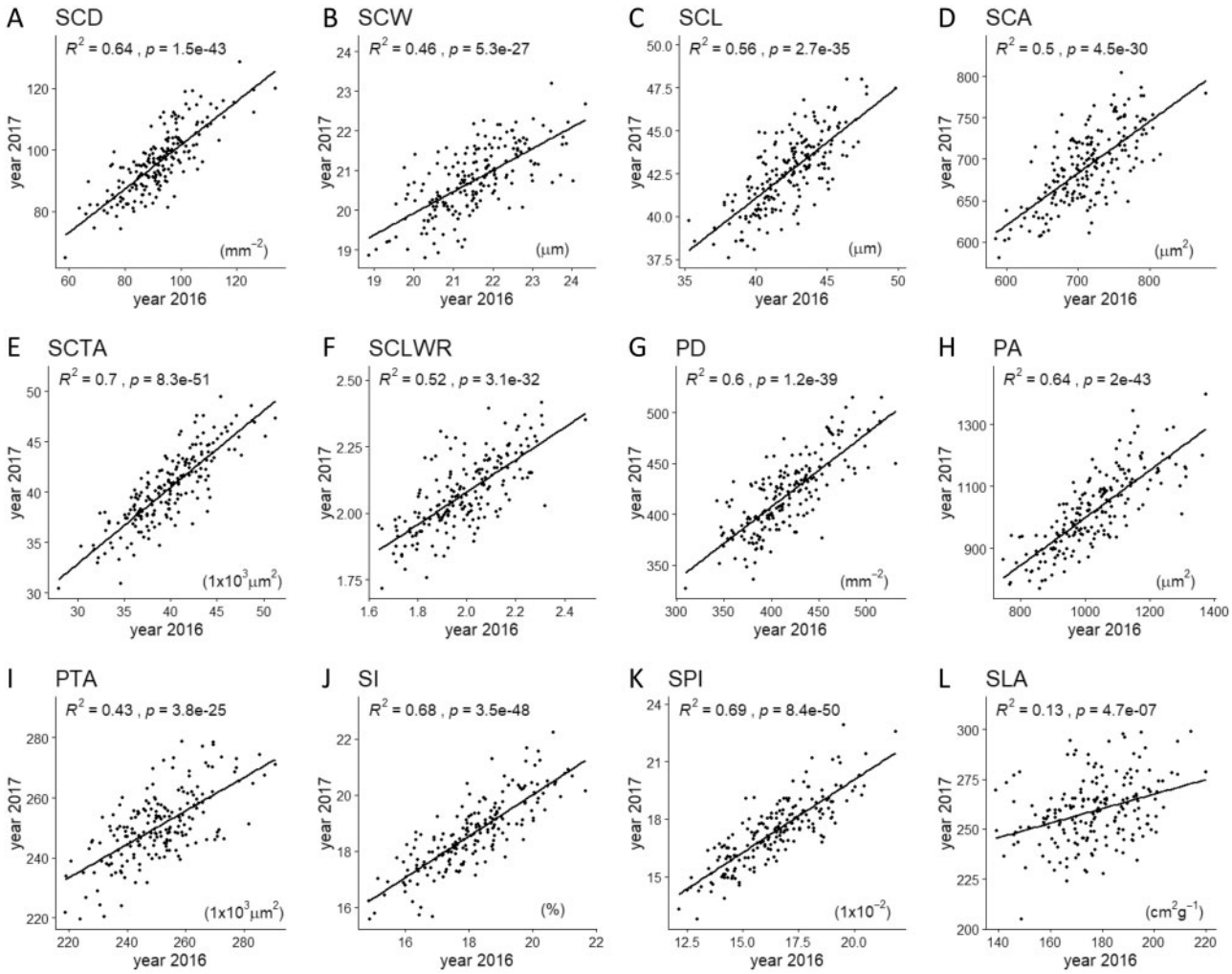

Figure 5 Scatterplots of genotype means for leaf anatomical traits of 191 maize B73 × MS71 RILs grown during the 2016 versus 2017 field seasons. SCD (A); SCW (B); SCL (C); SCA (D); SCTA (E); SCLWR (F); PD (G); PA (H); PTA (I); SI (J); SPI (K); SLA (L). The line of best fit (black line), coefficient of determination (R^2) and associated *P*-value are shown.

and was significant for SCW and *iWUE*. Six QTNs at 49–60 cM on chromosome 10 fall within the Chr10B cluster and are significant for SCW and g_s.

Discussion

Deep-learning has been proposed as a solution for a wide variety of applications in plant phenotyping (Ubbens and Stavness, 2017; Mochida et al., 2018; Jiang and Li, 2020; Singh et al., 2018). Despite this promise and publication of a number of tools, no solution has been widely adopted to assess stomatal patterning. This study successfully met the goals of building, testing, and demonstrating the use of a high-throughput phenotyping pipeline, including automated image analysis by use of machine learning for stomatal patterning traits in a model C_4 species. This was applied to 2 years of samples taken from a field-grown RIL population to advance understanding of the genetic architecture and trait relationships of stomatal patterning and leaf photosynthetic gas exchange in maize. Understanding of genetic variation in stomatal development and function is particularly poor in C_4 species. As such, the study addresses both technical and biological knowledge gaps that have been long-standing despite the considerable advances in understanding stomatal biology that have been made in recent years (Lawson and Vialet-Chabrand, 2019; Harrison et al., 2020; McKown and Bergmann, 2020).

High-throughput phenotyping pipeline for stomatal patterning traits

Data acquisition

OT was an effective method for imaging the leaf epidermis of maize RILs that displayed phenotypic diversity (Figure 2; Supplemental Figure S1) equal to, or greater than, that observed in the maize NAM founders (Supplemental Figure S9), Setaria RILs (Prakash et al., 2020) or 869 diverse sorghum accessions (Ferguson et al., manuscript in review). This proof-of-concept built upon previous applications in individual genotypes of Arabidopsis (Haus et al., 2018), tobacco (*Nicotiana tabacum*; Głowacka et al., 2018), and other dicot species (Haus et al., 2015). Each field of view could be

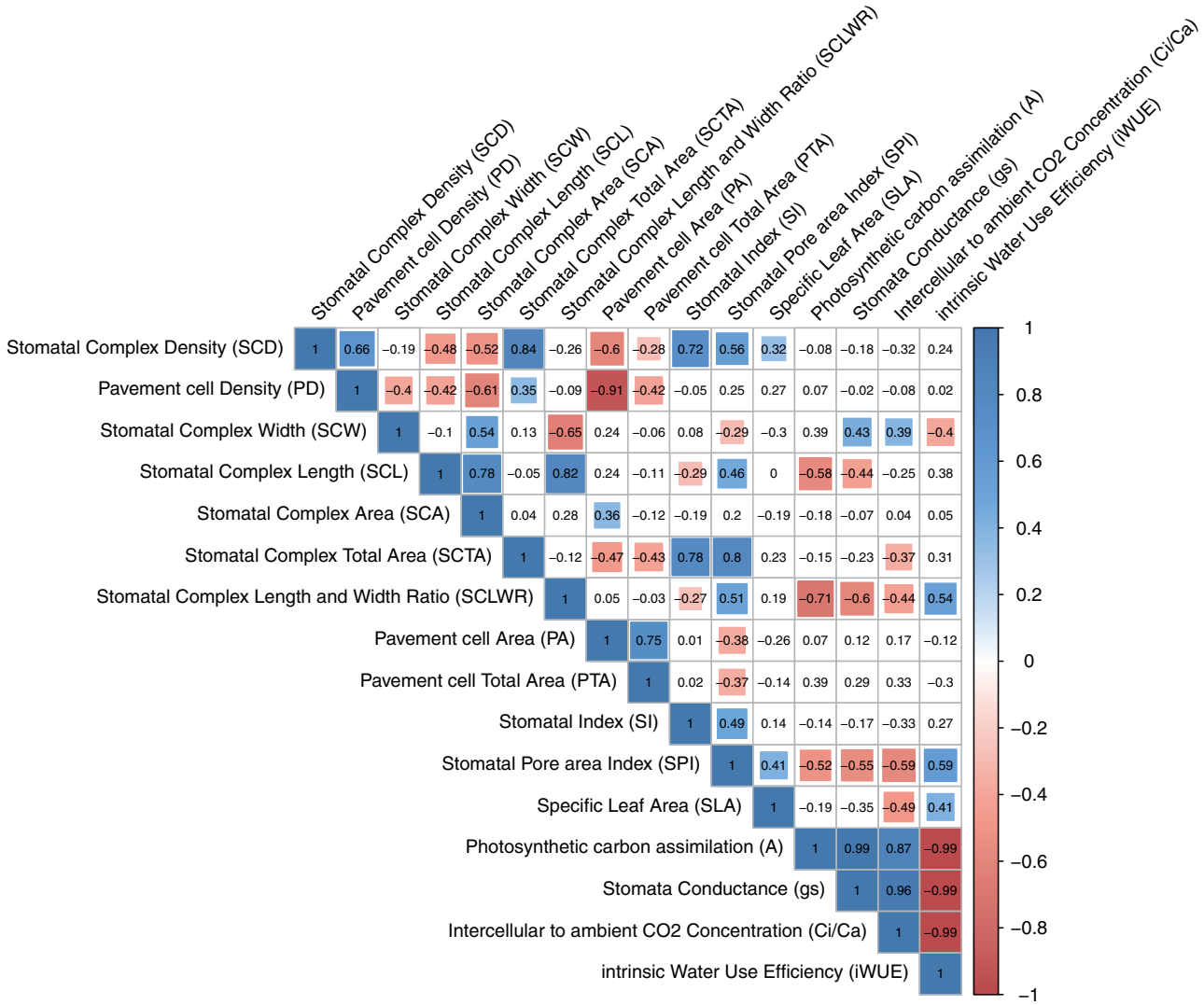

Figure 6 Genetic correlation matrix for SCD, SCW, SCL, SCLRW, SCA, SCTA, PD, PA, PTA, SI, SPI, SLA, rate of photosynthetic CO_2 assimilation (A), stomatal conductance (g_s), ratio of leaf intercellular to atmospheric CO_2 concentration (c_i/c_a) and *iWUE*, based on genotype means of the maize B73 × MS71 RIL population plus parental lines grown in 2017 ($n = 194$). Statistically significant correlations (p.adjust < 0.1) are highlighted with colored cells that reflect the strength of the correlation by the size of the shaded area and are colored from blue (positive correlation, coefficient $= 1$) to red (negative correlation, coefficient $= -1$).

acquired in <1 min, so sampling four or five fields of view per leaf allowed 60 leaves to be comfortably screened with a single microscope in a standard 8-h workday. This was more efficient and less arduous than our experience of taking leaf impressions or epidermal peels.

Data describing 11 different traits (Table 2) related to stomatal patterning were all significantly correlated across the two growing seasons, and with moderate to high heritability ($h^2 = 0.42–0.82$; Supplemental Table S1) despite variation in the growing environment in the field (Figure 5; Supplemental Figure S10). And, this led to consistent findings on trait relationships and the genetic architecture of stomatal traits across the years (Figures 6 and 7; Supplemental Figures S4 and S5).

Image analysis

The Mask R-CNN machine learning tool was successfully trained to automatically locate cells, identify cell classes, segment boundary coordinates, and extract density and size traits for stomata as well as pavement cells of maize leaf epidermis. Automatic image analysis was more than 100 times faster than manual measurement of the trait set (Table 1). Correlations between the number of stomata and pavement cells identified and counted by the computer versus expert humans were very strong ($r^2 > 0.96$) and showed little bias (Figure 3, A and B). This reflected robust predictions across a range of cell morphologies and image qualities, including for partial cells on image edges, and pavement cells above veins (Supplemental Figure S1). A second validation step

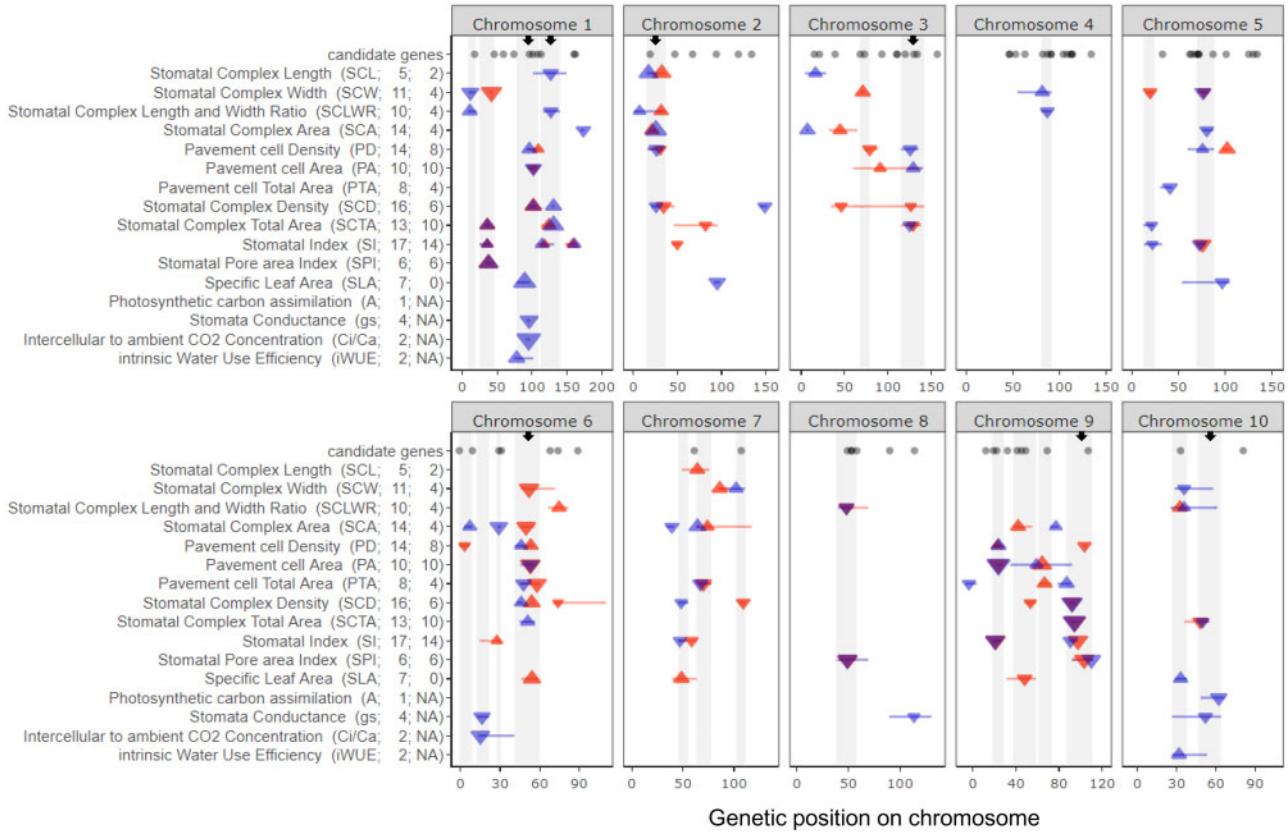

Figure 7 QTL mapping for SCD, SCW, SCL, SCLWR, SCA, SCTA, PD, PA, PTA, SI, SPI, SLA, rate of photosynthetic CO_2 assimilation (A), stomatal conductance (g_s), ratio of leaf intercellular to atmospheric CO_2 concentration (c_i/c_a), and *iWUE* from the B73 × MS71 RIL population. Each panel corresponds to an individual chromosome, where the values on the *x*-axis are chromosome position (cM). Numbers in parentheses following abbreviated trait names on the *y*-axis indicate the total number of QTL for that trait detected across the two growing seasons and the number of QTL for that trait that were detected consistently across both growing seasons. Each triangle represents a single QTL detected, with the direction of the arrow corresponding to the directional effect of the MS71 allele. Triangles are colored to indicate QTL that were significant in 2016 (red), 2017 (blue), or overlapping across both years (purple). Error bars indicate the 1.5 LOD support intervals. Gray shaded areas indicate clusters of colocated QTL. The location of putative orthologs of known stomatal patterning genes in Arabidopsis are indicated with gray dots. Black arrow at the top denotes potential evidence for pleiotropy within the QTL cluster.

that analyzed all available images for six genotypes that represented the range of SCD and PD in the RIL population suggests the variance mainly came from biological replicates, instead of technical errors (Figure 3, C and D). So, the pipeline produced equivalent or higher quality data much more rapidly.

Correlations between computer-generated estimates and human assessment of traits describing stomatal complex size were also highly significant (Figure 4). This aided detection of consistent results across seasons (Figure 5), and was achieved despite the additional challenge of stomatal size varying less across the RIL population (∼50%) than SCD (>100%). Nonetheless, accurate and precise estimation of stomatal size, and SCW in particular, pushed the limits of image resolution when data were collected with the 20X objective lens used in this study. Although this approach did allow many QTL and trait relationships to be identified, additional imaging using higher magnification lenses to deliver greater resolution from the OT will likely deliver further gains in the phenotyping of these traits. But, higher magnification is not ideal in all regards because fewer cells were observed and the proportion of leaf surface sampled were reduced.

The pipeline represents a valuable technical advance because previously published automatic stomatal detection and counting algorithms: (1) used data that were collected by slow and laborious methods (e.g., Aono et al., 2019; Bhugra et al., 2019; Sakoda et al., 2019); (2) were limited to detecting stomata and not pavement cells (e.g., Dittberner et al., 2018; Fetter et al., 2019; Li et al., 2019; Sakoda et al., 2019); (3) did not achieve the same accuracy (e.g., Duarte et al., 2017; Saponaro et al., 2017; Bourdais et al., 2019); or (4) were demonstrated to work only within the constrained variation of a limited sample set, which did not include demonstrated applicability for quantitative genetics (e.g., Aono et al., 2019; Fetter et al., 2019; Li et al., 2019). Although previous studies achieved these goals individually, combining these features resulted in a tool that could be applied to addressing knowledge gaps about the genetic architecture and trait relationships of epidermal cells in maize.

The independent application of the same tool to stomatal counting in grain sorghum suggests that, with the appropriate training, it has the flexibility and power to be widely applicable (Bheemanahalli et al., manuscript in review). But, as with all machine learning solutions to image analysis, there are significant questions about the context specificity of the model used. In the current study, the focus was on the development of a method that was robust across a RIL population of a model C_4 grass species, which included significant variation in many patterning traits but was also subtle relative to large datasets that span many species (Sack et al., 2003). Additional work will be needed to test if new models need to be trained for each individual mapping population or species of interest. One option may be transfer learning methods (Singh et al., 2018) to accelerate the development of machine learning models for new species or even a generic model. Even if this is not possible, training the Mask R-CNN tool required relatively few training instances (33 images containing roughly 2,000 cells for stomatal traits and 9,000 cells for pavement cell traits). So, building new models for different applications should be a tractable goal.

Trait variation across the RIL population and years

SCD of maize B73 × MS71 RILs showed a similar range to intraspecific variation in faba bean (Khazaei et al., 2014), wheat (Schoppach et al., 2016; Shahinnia et al., 2016), Arabidopsis (Dittberner et al., 2018), rice (Kulya et al., 2018; Laza et al., 2010), Setaria (Prakash et al., 2020), and sorghum (Ferguson et al., manuscript in review). Mean SCD and SCL of the RIL population were very similar to the abaxial trait values for maize and in the mid-range of a diverse set of species previously reported by McAusland et al. (2016). Therefore, maize does not represent an unusual extreme in terms of epidermal phenotype. Thus, the methods and biological discoveries here may relate to other species. Although, further comparative work is needed as grass epidermal patterning is distinct from that of dicots, and C_4 species may be expected to differ from C_3 relatives as a result of broader differences in leaf development and function associated with Kranz anatomy and associated biochemical specialization (Larkin et al., 1997).

The temperature of the 2017 growing season was similar to 2016, but there was ∼43% less precipitation (Supplemental Figure S10). Although this would be normally expected to drive plasticity in stomatal patterning traits, irrigation was applied to avoid plant drought stress in 2017. As a result, all epidermal patterning traits were moderately to highly heritable over the 2 years (h^2 = 0.42–0.82, Figure 5; Supplemental Table S1). SLA differed between years, probably as a result of harvesting material directly from the field in 2016 (low SLA due to high nonstructural carbohydrate content) versus after leaves had been held in the laboratory for photosynthetic gas exchange measurements in 2017 (higher SLA after starch reserves were respired under low light conditions in the laboratory). Nonetheless, genetic variation in SLA was correlated across years and relationships between SLA and other traits were similar across years. Therefore, the resulting data for all traits should be highly amenable for studying trait relationships and QTL mapping. Getting such information under mesic conditions without significant drought stress is valuable because it reduces the likelihood of complex plant–environment interactions that can complicate investigation of genetic variation in *iWUE* and associated traits (Leakey et al., 2019).

Trait relationships

A set of robust trait relationships were identified across years and across analyses of phenotypic and genetic correlation. Associations between stomatal patterning traits and leaf gas exchange rates were stronger in genetic correlations than phenotypic correlations. This suggests a common genetic basis for variation in stomatal patterning and *iWUE* that was partially obscured by environmental variation in the experiment. Traits related to the size and proportions of stomatal complexes were genetically correlated with *iWUE*, including SPI (r_g = 0.59), SCLWR (r_g = 0.54), and SCW (r_g = −0.40). This coincided with lower g_s being associated with longer, narrower stomatal complexes (Figure 6). This would be consistent with the morphology of the stomatal pore, and/or the guard cells and subsidiary cells that surround it, playing an important role in determining steady-state gas fluxes (Harrison et al., 2020). The dimensions of stomatal complexes have provided information about the maximum size of stomatal pores, in previous reports on C_4 grasses (Taylor et al., 2012) and tomato (Fanourakis et al., 2015). Overall, the structure–function relationships of stomatal size-WUE in C_4 species may parallel those previously reported in Arabidopsis (Des Marais et al., 2014; Dittberner et al., 2018). Nevertheless, the influence of stomatal size and shape on steady-state gas exchange is less well understood than its influence on the dynamics of stomatal opening and closing, so is worthy of further study (McAusland et al., 2016). Full understanding of how stomatal patterning traits impact g_s will likely depend on direct measurement of stomatal aperture under physiologically relevant conditions. It is also possible that variation in stomatal patterning between abaxial and adaxial leaf surfaces influenced g_s in a way that was not captured in the dataset on abaxial traits reported here. But there are ∼50% more stomata on the abaxial surface, so it should exert more influence. And, SI of the two leaf surfaces covary across diverse maize inbred lines (Foley 2012).

SCLWR was not associated with variation in PD, PA, or PTA (Figure 6). This opens up the possibility that the shape of stomatal complexes might be manipulated by breeding or biotechnology with minimal unpredictable side effects on epidermal patterning in general. However, further phenotyping advances will be needed to distinguish the contributions of guard cells versus subsidiary cells to these changes in stomatal complex size and proportions. The detailed information on epidermal cell allometry provided by the OT images and machine learning algorithm used in this study did reveal that PA and SCA are positively genetically correlated, as are SCD and PD (Figure 6). This is consistent with genetic

variation in cell size being general in nature across the two classes of epidermal cell types. However, this occurs at the same time as the tradeoff between SCD and SCA. So, a decrease in SCD appears to coincide with a compensatory increase in PA to fill the available space rather than an increase in PD. And, while SCL and SCW both drive variation in SCA, they are not correlated with each other, and they have opposing relationships with SI, SPI, SLA, and the gas exchange traits (Figure 6). Evaluating how stomatal complex size and proportion varies when SCD is manipulated transgenically may help reveal the key interdependencies between traits.

There was no significant correlation between SCD and g_s or any other gas exchange trait. Despite the classic tradeoff between SCD and measures of stomatal size being observed, this negative result contrasts with the widely held expectation that greater g_s will be associated with larger numbers of smaller stomata (Dow et al., 2014; Faralli et al., 2019). This expectation is strongly grounded in theory and data from broad fossil-based comparisons over phylogenetic space and geological time (Franks and Beerling, 2009). Significant relationships between SCD and water fluxes have also been observed in experiments on intraspecific variation in sorghum (Muchow and Sinclair, 1989), rice (Panda et al., 2018), and barley (Miskin et al., 1972). But, there are also a number of studies where SCD was not correlated with g_s in wheat (Liao et al., 2005), rice (Ohsumi et al., 2007), and barley (Jones, 1977). This discordance among studies, and the relatively weak nature of the relationship between SCD and g_s that is observed when it does occur within species, indicates how incompletely these structure–function relationships are understood. Therefore, the high-throughput phenotyping methods presented here, which can allow analysis across more and different types of genetic variation, will be valuable. One benefit of testing trait relationships within a RIL population is that the recombination of parental alleles resulting from making crosses breaks up gene linkage that can result from selection and underlie trait relationships, providing a more direct test of the biophysical basis for trait relationships (Des Marais et al., 2013). But the population also contains a limited portion of the overall genetic variation in the species, and results may reflect trait variation specific to the contrast between the B73 and MS71 parental lines.

Understanding the basis for genetic variation in *iWUE* is important because of the benefits to crop productivity, sustainability, and resilience that result from improving this key resource use efficiency (Leakey et al., 2019). Greater *iWUE* was strongly associated with lower g_s and more weakly associated with lower *A* (Figure 6). This was consistent with studies on sorghum (Kapanigowda et al., 2013; Ferguson et al., manuscript in review) and switchgrass (Taylor et al., 2016), although the strength of the correlations in this maize RIL population was significantly stronger. Whether *A* or g_s is the greater source of variation in *iWUE* has varied among studies, and approached equivalence when sufficient diversity was studied in wheat (Condon et al., 2004). Further work will be needed to see if the same pattern plays out in C_4 species, or whether g_s will remain the dominant driver of genetic variation in *iWUE* (Kapanigowda et al., 2013; Yasir et al., 2013; Taylor et al., 2016; Ferguson et al., manuscript in review).

QTL mapping and univariate/multivariate tests for pleiotropy

Of 63 QTL identified in 2016 and 77 QTL identified in 2017, 36 were consistently observed in both years (Figure 7). In addition, 24 clusters of overlapping QTL for multiple traits were identified. The number and strength of QTL identified for leaf gas exchange traits (1–4 QTL per trait in a single experiment) were similar to previous studies of those traits (Hervé et al., 2001; Teng et al., 2004; Pelleschi et al., 2006). In contrast, a greater number of QTL were identified for many of the stomatal patterning traits (e.g., PD—7, SI—9, SCA—9, SCD—9, SCTA—7 QTL in a single experiment) than in previous studies (Patto et al., 2003; Hall et al., 2005; Laza et al., 2010; Schoppach et al., 2016; Shahinnia et al., 2016; Liu et al., 2017; Sumathi et al., 2018; Delgado et al., 2019; Prakash et al., 2020). This larger number of significant QTL was linked to more small-effect QTL (PVE $<$ 10%) being successfully identified. This was unlikely to be the result of false positives because of the consistency in results across the 2 years of experimentation. This is valuable given the broad evidence suggesting that these stomatal patterning traits are likely to be polygenic, with multiple small-effect alleles combining to drive phenotypic variation (Schoppach et al., 2016; Shahinnia et al., 2016; Dittberner et al., 2018; Prakash et al., 2020; Bheemanahalli et al., manuscript in review; Ferguson et al., manuscript in review). This in turn corresponds with many genes being implicated in the network regulating cell fate during the differentiation of the epidermis, and therefore stomatal patterning (Pillitteri and Torii, 2012; McKown and Bergmann, 2020).

Loci that are pleiotropic for stomatal patterning and either g_s, c_i/c_a or *iWUE* are of interest as potential markers to select for improved *iWUE* or in the search for genes that underpin variation in the traits of interest. No statistical model alone can provide a definite answer of whether an association is caused by pleiotropy or linkage. However, based on the univariate results obtained by Fernandes et al. (2021) on simulated traits, the proportion of simultaneously detected QTNs is only as high as the detection of the QTN for each trait individually under pleiotropy or tight linkage, which in many cases would have the same implications as pleiotropy for breeding purposes. In this context, the detection of a given SNP in 100% of the univariate analysis indicates a multitrait association. The multivariate results provide another piece of evidence in favor of the possible pleiotropic association. Therefore, although a validation study where crossing is performed to recombine alleles within the region of interest would be required to exclude the possibility of linkage, the results we obtain provide a short list of putatively pleiotropic QTNs (Supplemental Table S4). Using this approach,

one locus on chromosome 1 and two loci on 10 were identified as having the greatest potential to be pleiotropic for stomatal patterning and g_s or *iWUE* (Supplemental Table S4). In addition to containing QTL that explain 8%–10% of the variation in *iWUE*, clusters Chr1C and Chr10A contain QTL that are amongst the strongest for SCD (PVE = 11%), SCW (PVE = 8%) and SCWLR (PVE = 6%), respectively (Supplemental Table S2). More broadly, the QTL for different structural and functional traits within these regions had allelic effects consistent with each other and the overall trait relationships observed in the population. And, while QTL intervals are too large to allow the causal genes underlying the genotype–phenotype association to be identified with confidence, it was possible to determine whether putative pleiotropic QTL did or did not overlap with the locations of known stomatal developmental genes in maize or putative orthologs of known stomatal patterning genes in Arabidopsis (Supplemental Table S2).

S_181051496 on chromosome 1 stands out as a putatively pleiotropic QTN that is significantly associated with SCD, PD, SCTA, PA, SPI, SLA, g_s, and c_i/c_a. A putative ortholog of EPIDERMAL PATTERNING FACTOR 2 (EPF2, GRMZM2G051168) is found at the same genetic position, while PANGLOSS1 (PAN1, GRMZM5G836190) is located 5 cM away (Supplemental Table S2). PAN1 regulates subsidiary mother cell divisions (Cartwright et al., 2009), while EPF2 is a negative regulator of the number of stomata (Hara et al., 2009), which has been overexpressed to increase WUE in a number of species (Harrison et al., 2020).

S_15690240 was identified as a putatively pleiotropic QTN that was significantly associated with SCW and *iWUE*. It is colocalized with the putative maize ortholog of Arabidopsis A2-type cyclin CYCA2;1 (GRMZM5G879536). RNAi knockdown of OsCYCA2;1 in rice led to significantly reduced stomatal production, but did not disrupt guard mother cell division, as was the case in Arabidopsis (Vanneste et al., 2011; Qu et al., 2018). If confirmed, the involvement of these genes, and others in Supplemental Table S2, in regulating stomatal patterning in maize would be consistent with the notion that the same set of genes regulates cell fate to control stomatal patterning in dicots and monocots, but the roles of individual genes within the network have been modified over the course of evolutionary time (Raissig et al., 2016, 2017; Wu et al., 2019).

At the same time, the identification of multiple high-confidence QTL that do not overlap with existing candidate genes also suggests the possibility that additional genes regulating stomatal patterning remain to be discovered and high-throughput phenotyping of stomatal patterning could aid in their discovery. Six putatively pleiotropic QTNs (S_126261991, S_127997890, S_131319540, S_131939239, S_133322225, S_135943280) colocated with QTL cluster Chr10B were all associated with both SCW and g_s. This presents an opportunity to further investigate the genetic basis for links between stomatal complex size, g_s, and *iWUE*. Stomatal size has recently received attention as a target for improving *iWUE* through altered rates of opening and closing (Lawson and Blatt, 2014; Pignon et al., 2021). Despite this, and a theoretical basis for it to impact steady-state g_s (Dow et al., 2014), the genetic basis for variation in stomatal size or stomatal dimensions is much less understood than variation in SCD.

The discovery of multiple QTL for stomatal patterning traits suggests that the goal of reducing g_s and improving *iWUE* by reducing SCD or increasing SCLWR could be achieved through breeding to combine alleles that would result in more extreme trait values than were found in either of the parental inbred lines. This is particularly the case when not all MS71 alleles were associated with, for example, lower SD. Further work is needed to test that possibility and also to experimentally confirm if the loci identified here are truly pleiotropic versus being multiple loci in linkage.

Conclusion

This study presents an end-to-end pipeline for high-throughput phenotyping of stomatal patterning. Insights were generated on trait relationships within and between stomatal anatomical features and leaf photosynthetic gas exchange. The genetic architecture and trait relationships of stomatal patterning and leaf gas exchange traits were characterized in detail. These insights lay the groundwork to (1) apply the high-throughput phenotyping pipeline to other experiments taking quantitative genetics, reverse genetics, or forward genetics approaches and (2) further investigate the physiological and genetic basis for variation in stomatal development, stomatal conductance, and *iWUE* in C_4 species, which is poorly understood despite the agricultural and economic significance of these crops.

Materials and methods

Plant material and sampling

Field experiments were done on the University of Illinois at Urbana-Champaign South Farms in Savoy, IL (40°02′N, 88°14′W). Maize (*Zea mays*) seeds were planted on 24 May 2016 and 17 May 2017 with a planting spacing in each row of 8 plants/m and row spacing of 0.76 m. The crop was grown in rotation with soybean (*Glycine max*) and received 200 kg/ha of nitrogen fertilizer. A population of RILs derived from a B73 × MS71 cross was grown, with 197 RILs planted in 2016 and 192 RILs plus the parental lines planted in 2017. This population is a subset of the maize Nested Association Mapping (NAM) population (Yu et al., 2008) and was selected as a result of the parent lines having low (MS71) and moderate SCD (B73) compared to the other inbred founder lines in an initial screen performed at the same field site (Supplemental Figure S9). Seeds were obtained from the Maize Genetics Cooperation Stock Center (University of Illinois Urbana-Champaign). In 2016, four replicate plants were sampled at random from within the middle portion of nursery rows, which were also self-fertilized for seed production. In 2017, a randomized complete block design was used with two blocks, each containing a replicate plot for each

RIL and six replicate plots for each parental line. Two subsamples were collected from separate plants in all replicate rows. In 2017 the field was equipped with drip tape and irrigation was applied uniformly across all genotypes whenever early signs of drought stress were observed. Temperature and precipitation were recorded by the Water and Atmospheric Resources Monitoring Program (Supplemental Figure S10). (Illinois Climate Network, 2019. Illinois State Water Survey, 2204 Griffith Drive, Champaign, IL 61820-7495. http://dx.doi.org/10.13012/J8MW2F2Q.)

In both years, measurements were taken on the second leaf beneath the flag leaf following anthesis. In 2016, collection of leaf samples for phenotyping epidermal cell patterning and SLA was done in the field. In 2017, tissue sampling was performed after photosynthetic gas exchange measurements were done on the leaves. For this, leaves were cut early in the morning at the base of the leaf blade distally adjacent to the ligule. Cut ends were then submerged in buckets of water and transported to the laboratory. The leaves were then recut under water and remained in 50 mL tubes of water during measurements of gas exchange and tissue sampling.

Epidermal image acquisition

To phenotype epidermal cell patterning, ~0.5 cm-wide strips were excised from the margin to the mid-rib at a point halfway along the length of a leaf using scissors. Samples were immediately stored in a 2 mL tube, flash frozen in liquid nitrogen, and stored at −20°C. Leaves were flattened and stabilized onto glass slides with double-sided tape immediately prior to imaging. Abaxial surfaces were imaged with a Nanofocus µsurf Explorer Optical Topometer (Oberhausen, Germany) at 20X magnification with 0.6 numerical aperture. The topography layer was constructed by stacking all the focused pixels across planes of the *Z*-axis. Output images were 0.8 mm × 0.8 mm on *x* and *y* axes (512 × 512 pixels). Five fields of view were scanned on each leaf sample in 2016 and four fields of view were scanned on each leaf sample in 2017. Fields of view were arranged equidistantly along a latitudinal transect from the leaf edge to mid-rib. Sample loss or poor sample quality resulted in incomplete replication for 22 RILs in 2016 and 2 RILs in 2017. Therefore, in total, 3,785 images were in the 2016 dataset and 3,248 images were in the 2017 dataset (Figure 1A).

The 3D topographic layer (Figure 2A) was input into Nanofocus µsurf analysis extended software (Oberhausen, Germany) for image processing as follows: first, nonmeasured points were filled by a smooth shape calculated from neighboring points. A Robust Gaussian filter with cutoffs of 200, 100, and 100 µm were applied in sequence (Figure 2B). Then, a Laplacian filter with a 13 × 9 pixel kernel size was implemented (Figure 2C) before applying another Robust Gaussian filter with a cutoff of 80 µm. The final 3D layer was then flattened to 2D in grayscale with auto-optimization for luminosity and contrast enhancement.

Mask R-CNN model training

Twenty-four images were initially randomly selected for training the Mask R-CNN model for object instance segmentation. Subsequently, nine additional images of pavement cells that overlie minor veins were added to the training set to improve the detection accuracy for these cells. Each stomatal complex and pavement cell was traced as an object instance using VGG Image Annotator (Dutta and Zisserman, 2019). A JavaScript Object Notation (.json) file was generated for each image to record the coordinates for all instance masks within that image. Json files of 26 randomly selected images were pooled to form the training set, and 7 images were pooled into a validation set (i.e., approximately 11,000 unique cells used for model training; Figure 1A). A Mask R-CNN repository built by Matterport Inc. on GitHub (Waleed, 2017) was used for training on a customized PC with a GeForce GTX 1080 Ti graphics processing unit and 32 GB of RAM. Model training was based on the ResNet-101 backbone with pretrained weights from the COCO dataset (Lin et al., 2014) with 50 epochs of 100 steps. The learning rate, learning momentum, and weight decay were 0.001, 0.9, and 0.0001, respectively. All images were flipped horizontally and vertically for augmentation. The process taken by Mask R-CNN to make predictions on the instances, size, and shape of pavement and stomatal cells are summarized in Figure 1B.

Epidermal cell detection, trait extraction, and evaluation

The model built during the training process was applied to the detection of cells in the entire image dataset, using the same software and hardware configurations. Instance coordinates and cell type predictions saved by the Mask R-CNN model as individual csv files were inputted into R for epidermal trait extraction. The number of stomatal complex and pavement cells within each image were derived as the number of instances detected for these two separate classes and they were standardized by image area to get SCD as well as PD. The areas of complete, individual stomatal complexes (SCA), and pavement cells (PA) were calculated based on the boundary coordinates using the *splancs* package (version 2.01-40). To derive the SCL and SCW, an ellipse was first fitted to each stomatal complex using *MyEllipsefit* package (version 0.0.4.2). SCW and SCL were calculated as doubling the radius along the minor and major axis, respectively (Figure 2G). The ratio of SCLWR was derived as SCL divided by SCW. SCTA and PTA were calculated as the sum of areas for all instances of these two cell types, including partial cells on the edge. Total SPI (Sack et al., 2003) is the product of SCD and SCL squared. SI was calculated as the number of stomatal complexes divided by the sum of stomatal complex number and pavement cell number. The *Imager* package (version 0.41.2) and *magick* package (version 2.0) were used to label cells and cell boundaries on detection output images for better visualization.

For validation of SCD and PD, a group of people received training on stomata and pavement cell recognition and

reached consensus on the criteria. Two sets of images that were not part of the training dataset were then manually assessed (Figure 1A). First, six people each manually measured 100 images selected at random from the 2016 and 2017 data. Second, five people each manually measured all images for six genotypes, chosen to represent the range of observed epidermal cell densities, selected from the 2016 dataset. Manual counting was done in Image J 1.8.0 (Schneider et al., 2012) using the multipoint tool. To validate predictions of stomatal size traits by Mask R-CNN, six humans each manually measured the same five stomatal complexes in each of 42 randomly selected images that were not part of the training dataset (Figure 1A).

Leaf photosynthetic gas exchange and SLA

In 2017, A, g_s, c_i/c_a, and *iWUE* were measured using four LI-6400 portable photosynthesis systems incorporating an infrared gas analyzer (LI-COR, Lincoln, NE, USA) that was run simultaneously using the protocol of Choquette et al. (2019). Rates of gas exchange measured in this manner have previously been shown to correspond well with in-situ measurements under well-watered conditions (Markelz et al., 2011; Wolz et al., 2017). In addition to being rapid, the approach benefits from avoiding short-term changes in water potential that occur in the field, and that may limit photosynthesis. Four leaf disks were sampled using a leaf punch from the same leaf sampled for stomata scanning. Leaf disks were dried in an oven at 60°C before being weighed on a precision balance (Mettler Toledo XS205, OH, USA). SLA ($cm^2\ g^{-1}$) was calculated as the area for leaf punch divided by the mean leaf disk weight.

Statistical analysis

All statistical analyses were performed in R (version 3.6.0, https://www.r-project.org). Pearson correlations were performed and visualized using the *corrplot* package (version 0.84). Genetic correlations between all pairwise traits were estimated by fitting bivariate models in ASReml-R v4.0 package (Butler et al., 2018) and modeling the genetic effect with correlation structure "corgh" as in (Fernandes et al., 2018). The standard error was obtained from this same model and estimated with the delta method. Finally, we fitted this same bivariate model with the "diag" variance–covariance structure. Since the only difference between the structures "diag" and "corgh" is the correlation term, we tested the two models with a likelihood ratio test to obtain a *P*-value for the genetic correlation. The kinship was calculated with the function A.mat() from the package rrBLUP (Endleman, 2011). The genotype data were numericalized using the most frequent allele as the reference one. It was done on the function as_numeric() from the package simplePHENOTYPES (Fernandes and Lipka, 2020). Multiple testing correction was implemented based on Benjamini–Hochberg procedure and a false discovery rate of 10%. In the calculation of broad-sense heritability estimations, a linear mixed model was fitted for each trait treating "genotype" effect as random. Heritability was then estimated as the proportion of genotypic variation among the total variation across 2 years.

The genetic map for B73 × MS71 population consists of 1,478 SNPs distributed across all 10 chromosomes of maize (McMullen et al., 2009). SNP data were available as part of the Maize Diversity Project (https://www.panzea.org). Markers were phased and imputed to a density of 1 cM resolution. QTL mapping for 2 years was done separately and performed in R for each individual trait using the *stepwiseqtl* function with Haley–Knott algorithm from package *qtl* (Broman et al., 2003) to create a multiple QTL model. A multilocus model was generated using stepwise forward selection and backward elimination. The maximum number of QTL limited in the forward selection was set as 10. The Logarithm of the odds (LOD) penalties for QTL selection was calculated using the *scantwo* function with 1,000 permutations for each trait at a significance level of 0.05. LOD scores and PVE values were estimated using *fitqtl* function. Following Dupuis and Siegmund (1999) and Banan et al. (2018), 1.5-LOD support intervals were used for each QTL hit. Colocalized QTL were grouped into "clusters" based on their mapping to the same or neighboring markers where confidence intervals overlapped. The few QTL with very large confidence intervals (>50 cM) were excluded from clusters. Clusters were named in sequence order (Figure 7; Supplemental Table S2; e.g., Chr1A–Chr1D for clusters on chromosome 1 based on their genetic position). Maize 5b gene model coordinates and annotations were both downloaded from MaizeGDB (https://www.maizegdb.org).

A series of univariate and multivariate single marker analyses were done to assess the evidence for pleiotropic causal mutations underlying the statistical associations initially identified as overlapping QTL in a given region of a chromosome. For each trait, a univariate linear regression using 80% of the data was performed, where a given trait was the response variable and a single SNP was the explanatory variable. This process was repeated 100 times, with different individuals sampled each time. Next, the proportion of times that a given SNP passed the *P*-value threshold of 0.05 was measured. For each SNP that passed the threshold in all replicates (i.e., a proportion of 100%) for more than one trait, a multivariate linear regression model was run with these traits as the response variable, and that SNP as the explanatory variable.

The multivariate analysis was performed using 80% of the data in each of the 100 replicates. In each replicate, the same individuals used in the univariate analysis were used in the multivariate one. These results were also filtered to only keep SNPs passing the threshold in 100% of the replicates in the multivariate analysis. For multitrait models in which more than one SNP was retained, another multivariate analysis was run with all SNPs included in the model. All the SNPs with a *P*-value smaller than 0.05 after the inclusion of all other retained SNPs were reported as putatively pleiotropic QTNs (Supplemental Table S4).

Data availability

Data availabilityOptical tomography images from this article can be found in the Illinois Data Bank under https://doi.org/10.13012/B2IDB-8275554_V1.

Supplemental data

The following materials are available in the online version of this article.

Supplemental Figure S1. Examples of input images and the predictions of cell instances made for them across a range of epidermis morphology and image qualities.

Supplemental Figure S2. Scatterplots of variation among six expert human evaluators in manual measurements of stomatal patterning traits from 100 randomly selected OT images from the B73 × MS71 maize RIL population.

Supplemental Figure S3. Frequency distributions of leaf traits for the maize B73 × MS71 RIL population grown in 2016 (gray) and 2017 (yellow).

Supplemental Figure S4. Genetic and phenotypic correlation matrices for epidermal anatomy and leaf gas exchange traits based on genotype means of the maize B73 × MS71 RIL population grown in 2016 ($n = 197$).

Supplemental Figure S5. Phenotypic correlation matrix for epidermal anatomy and leaf gas exchange traits based on genotype means of the maize B73 × MS71 RIL population grown in 2017 ($n = 194$).

Supplemental Figure S6. Scatter plot of photosynthetic carbon assimilation (A_n) versus stomata conductance (g_s) measured in year 2017. Each point denotes a RIL.

Supplemental Figure S7. Manhattan plots showing significant QTL for each trait detected in year 2016 (red) and year 2017 (blue).

Supplemental Figure S8. Sum of percentage of variance explained (PVE) for all QTL identified for each trait in 2016 (gray bars) and 2017 (yellow bars).

Supplemental Figure S9. Initial screening of SCD (A), PD (B), and SI (C) for maize NAM population founder lines grown in year 2014 ($n = 4$).

Supplemental Figure S10. Daily mean temperature (brown line; °C) and water inputs to field trials (blue bars = total daily precipitation, red bars = irrigation; mm) in Savoy, Illinois for each day of year (DOY).

Supplemental Table S1. Broad sense heritability estimations for epidermal anatomical traits across years.

Supplemental Table S2. Detailed QTL information for each hit, grouping of QTL clusters, and overlapping candidate genes.

Supplemental Table S3. Detailed QTL information for QTL interactions.

Supplemental Table S4. List of SNPs that passed the *P*-value threshold of 0.01 in all 100 resamples used on univariate and multivariate regression.

Acknowledgments

We thank Anthony Studer for helpful discussions on QTL mapping and Elizabeth Ainsworth for comments on a draft manuscript. We thank Patrick Brown, Christopher Montes, Crystal Sorgini, and Benjamin Thompson for assistance with acquisition of germplasm, as well as establishment and maintenance of field plots. We thank Timothy Wertin, Nicole Choquette, Jim Berry, Aya Bridgeland, and Chris Moller for assistance with sample and data collection. We thank Bindu Edupulapati, Kayla Raflores, Varun Govind, and Vishnu Chavva for assistance with manual assessment of stomatal traits in OT images.

Funding

This work was supported by the National Science Foundation (grant no. PGR-1238030), Agriculture and Food Research Initiative (AFRI; grant no. 2020-67021-32799/project accession no.1024178) from the USDA National Institute of Food and Agriculture, and the University of Illinois Center for Digital Agriculture, and a Foundation for Food and Agriculture Research Graduate Student Fellowship (to J.X.).

Conflict of interest statement. None declared.

References

Alter RE, Douglas HC, Winter JM, Eltahir EAB (2018) Twentieth century regional climate change during the summer in the central United States attributed to agricultural intensification. Geophys Res Lett **45**: 1586–1594

Aono AH, Nagai JS, Dickel SM, Marinho RC (2019) A stomata classification and detection system in microscope images of maize cultivars. bioRxiv https://doi.org/10.1101/538165

Banan D, Paul RE, Feldman MJ, Holmes MW, Schlake H, Baxter I, Jiang H, Leakey ADB (2018) High-fidelity detection of crop biomass quantitative trait loci from low-cost imaging in the field. Plant Direct **2**: e00041

Bergmann DC (2004) Integrating signals in stomatal development. Curr Opin Plant Biol **7**: 26–32

Bhugra S, Mishra D, Anupama A, Chaudhury S, Lall B, Chugh A, Chinnusamy V (2019) Deep convolutional neural networks based framework for estimation of stomata density and structure from microscopic images. *In* Lecture Notes in Computer Science (including subseries Lecture Notes in Artificial Intelligence and Lecture Notes in Bioinformatics) 11134 LNCS, pp 412–423

Biscoe TD (1872) The breathing pores of leaves. Am Nat **6**: 129–133

Blatt MR (2000) Cellular signaling and volume control in stomatal movements in plants. Annu Rev Cell Dev Biol **16**: 221–241

Bourdais G, McLachlan DH, Rickett LM, Zhou J, Siwoszek A, Häweker H, Hartley M, Kuhn H, Morris RJ, MacLean D, et al. (2019) The use of quantitative imaging to investigate regulators of membrane trafficking in Arabidopsis stomatal closure. Traffic **20**: 168–180

Broman KW, Wu H, Sen Ś, Churchill GA (2003) R/qtl: QTL mapping in experimental crosses. Bioinformatics **19**: 889–890

Buckler ES, Holland JB, Bradbury PJ, Acharya CB, Brown PJ, Browne C, Ersoz E, Flint-Garcia S, Garcia A, Glaubitz JC, et al. (2009) The genetic architecture of maize flowering time. Science **325**: 714–718

Butler DG, Cullis BR, GilmourAR, Gogel BG, and Thompson R (2018) ASReml-R Reference Manual Version 4. VSN International Ltd, Hemel Hempstead, HP1 1ES, UK

Caine RS, Yin X, Sloan J, Harrison EL, Mohammed U, Fulton T, Biswal AK, Dionora J, Chater CC, Coe RA, et al. (2019) Rice with reduced stomatal density conserves water and has improved

drought tolerance under future climate conditions. New Phytol **221**: 371–384

Campitelli BE, Marais DLD, Juenger TE (2016) Ecological interactions and the fitness effect of water-use efficiency: competition and drought alter the impact of natural MPK12 alleles in Arabidopsis. Ecol Lett **19**: 424–434

Cartwright HN, Humphries JA, Smith LG (2009) PAN1: a receptor-like protein that promotes polarization of an asymmetric cell division in maize. Science **323**: 649–651

Choquette NE, Ogut F, Wertin TM, Montes CM, Sorgini CA, Morse AM, Brown PJ, Leakey ADB, McIntyre LM, Ainsworth EA (2019) Uncovering hidden genetic variation in photosynthesis of field-grown maize under ozone pollution. Glob Change Biol **25**: 4327–4338

Condon AG, Richards RA, Rebetzke GJ, Farquhar GD (2004) Breeding for high water-use efficiency. J Exp Bot **55**: 2447–2460

Delgado D, Sánchez-Bermejo E, de Marcos A, Martín-Jimenez C, Fenoll C, Alonso-Blanco C, Mena M (2019) A genetic dissection of natural variation for stomatal abundance traits in arabidopsis. Front Plant Sci **10**: 1392

Des Marais DL, Auchincloss LC, Sukamtoh E, McKay JK, Logan T, Richards JH, Juenger TE (2014) Variation in MPK12 affects water use efficiency in Arabidopsis and reveals a pleiotropic link between guard cell size and ABA response. Proc Natl Acad Sci U S A **111**: 2836–2841

Des Marais DL, Hernandez KM, Juenger TE (2013) Genotype-by-environment interaction and plasticity: exploring genomic responses of plants to the abiotic environment. Annu Rev Ecol Evol Syst **44**: 5–29

Dittberner H, Korte A, Mettler-Altmann T, Weber APM, Monroe G, de Meaux J (2018) Natural variation in stomata size contributes to the local adaptation of water-use efficiency in Arabidopsis thaliana. Mol Ecol **27**: 4052–4065

Dow GJ, Berry JA, Bergmann DC (2014) The physiological importance of developmental mechanisms that enforce proper stomatal spacing in Arabidopsis thaliana. New Phytol **201**: 1205–1217

Duarte KTN, de Carvalho MAG, Martins PS (2017) Segmenting High-Quality Digital Images of Stomata using the Wavelet Spot Detection and the Watershed Transform, pp 540–547

Dupuis J, Siegmund D (1999) Statistical methods for mapping quantitative trait loci from a dense set of markers. Genetics **151**: 373–386

Dutta A, Zisserman A (2019) The VIA annotation software for images, audio and video. *In* Proceedings of the 27th ACM International Conference on Multimedia. Association for Computing Machinery, Nice, France, pp 2276–2279

Endleman JB (2011) Ridge regression and other kernels for genomic selection with R package rrBLUP. Plant Genome **4**: 250–255.

Fanourakis D, Giday H, Milla R, Pieruschka R, Kjaer KH, Bolger M, Vasilevski A, Nunes-Nesi A, Fiorani F, Ottosen CO (2015) Pore size regulates operating stomatal conductance, while stomatal densities drive the partitioning of conductance between leaf sides. Ann Bot **115**: 555–565

Faralli M, Matthews J, Lawson T (2019) Exploiting natural variation and genetic manipulation of stomatal conductance for crop improvement. Curr Opin Plant Biol **49**: 1–7

Fernandes SB, Dias KOG, Ferreira DF, Brown PJ (2018) Efficiency of multi-trait, indirect, and trait-assisted genomic selection for improvement of biomass sorghum. Theoretical and Applied Genetics **131**: 747–755

Fernandes SB, Lipka AE (2020) simplePHENOTYPES: SIMulation of pleiotropic, linked and epistatic phenotypes. BMC Bioinformatics **21**: 491. https://doi.org/10.1186/s12859-020-03804-y

Fernandes SB, Zhang KS, Jamann TM, Lipka AE (2021) How well can multivariate and univariate GWAS distinguish between true and spurious pleiotropy? Front Genet **11**: 602526. doi: 10.3389/fgene.2020.602526

Fetter KC, Eberhardt S, Barclay RS, Wing S, Keller SR (2019) StomataCounter: a neural network for automatic stomata identification and counting. New Phytol **223**: 1671–1681 doi: 10.1111/nph.15892

Foley RC (2012) The genetic diversity of water use efficiency in the nested associated mapping population of Zea mays. MSc thesis. Purdue University, West Lafayette, Indiana.

Franks PJ, Beerling DJ (2009) Maximum leaf conductance driven by CO_2 effects on stomatal size and density over geologic time. Proc Natl Acad Sci U S A **106**: 10343–10347

Franks PJ, W. Doheny-Adams T, Britton-Harper ZJ, Gray JE (2015) Increasing water-use efficiency directly through genetic manipulation of stomatal density. New Phytol **207**: 188–195

Głowacka K, Kromdijk J, Kucera K, Xie J, Cavanagh AP, Leonelli L, Leakey ADB, Ort DR, Niyogi KK, Long SP (2018) Photosystem II subunit S overexpression increases the efficiency of water use in a field-grown crop. Nat Commun **9**: 868

Hall NM, Griffiths H, Corlett JA, Jones HG, Lynn J, King GJ (2005) Relationships between water-use traits and photosynthesis in Brassica oleracea resolved by quantitative genetic analysis. Plant Breeding **124**: 557–564

Hara K, Yokoo T, Kajita R, Onishi T, Yahata S, Peterson KM, Torii KU, Kakimoto T (2009) Epidermal cell density is autoregulated via a secretory peptide, EPIDERMAL PATTERNING FACTOR 2 in arabidopsis leaves. Plant Cell Physiol **50**: 1019–1031

Harrison EL, Cubas LA, Gray JE, Hepworth C (2020) The influence of stomatal morphology and distribution on photosynthetic gas exchange. Plant J **101**: 768–779

Haus MJ, Kelsch RD, Jacobs TW (2015) Application of optical topometry to analysis of the plant epidermis. Plant Physiol **169**: 946–959. doi: 10.1104/pp.15.00613

Haus MJ, Li M, Chitwood DH, Jacobs TW (2018) Long-distance and trans-generational stomatal patterning by CO_2 across Arabidopsis organs. Front Plant Sci **9**: 1–11

He K, Gkioxari G, Dollar P, Girshick R (2017) Mask R-CNN. *In* Proceedings of the IEEE International Conference on Computer Vision, pp 2980–2988

Heichel GH (1971) Genetic control of epidermal cell and stomatal frequency in maize. Crop Sci **11**: 830–832. cropsci1971.0011183X001100060019x

Hepworth C, Caine RS, Harrison EL, Sloan J, Gray JE (2018) Stomatal development: focusing on the grasses. Curr Opin Plant Biol **41**: 1–7

Hervé D, Fabre F, Berrios EF, Leroux N, Chaarani GA, Planchon C, Sarrafi A, Gentzbittel L (2001) QTL analysis of photosynthesis and water status traits in sunflower (Helianthus annuus L.) under greenhouse conditions. J Exp Bot **52**: 1857–1864

Hetherington AM, Woodward FI (2003) The role of stomata in sensing and driving environmental change. Nature **424**: 901–908

Higaki T, Kutsuna N, Hasezawa S (2015) CARTA-based semi-automatic detection of stomatal regions on an Arabidopsis cotyledon surface. Plant Morphol **26**: 9–12

Hughes J, Hepworth C, Dutton C, Dunn JA, Hunt L, Stephens J, Waugh R, Cameron DD, Gray JE (2017) Reducing stomatal density in barley improves drought tolerance without impacting on yield. Plant Physiol **174**: 776–787

Jayakody H, Liu S, Whitty M, Petrie P (2017) Microscope image based fully automated stomata detection and pore measurement method for grapevines. Plant Methods **13**: 1–12

Jiang Y, Li C (2020) Convolutional neural networks for image-based high-throughput plant phenotyping: a review. Plant Phenomics **2020**: 4152816. doi: https://doi.org/10.34133/2020/4152816

Jones HG (1977) Transpiration in barley lines with differing stomatal frequencies. J Exp Bot **28**: 162–168

Kapanigowda MH, Perumal R, Djanaguiraman M, Aiken RM, Tesso T, Prasad PVV, Little CR (2013) Genotypic variation in sorghum [Sorghum bicolor (L.) Moench] exotic germplasm collections for drought and disease tolerance. SpringerPlus **2**: 650

Khazaei H, O'Sullivan DM, Sillanpää MJ, Stoddard FL (2014) Use of synteny to identify candidate genes underlying QTL controlling stomatal traits in faba bean (Vicia faba L.). Theor Appl Genet **127**: 2371–2385

Kulya C, L. Siangliw J, Toojinda T, Lontom W, Pattanagul W, Sriyot N, Sanitchon J, Theerakulpisut P (2018) Variation in leaf anatomical characteristics in chromosomal segment substitution lines of KDML105 carrying drought tolerant QTL segments. ScienceAsia **44**: 197

Larkin JC, Marks MD, Nadeau J, Sack F (1997) Epidermal cell fate and patterning in leaves. Plant Cell **9**: 1109–1120

Lawson T, Blatt MR (2014) Stomatal size, speed, and responsiveness impact on photosynthesis and water use efficiency. Plant Physiol **164**: 1556–1570

Lawson T, Simkin AJ, Kelly G, Granot D (2014) Mesophyll photosynthesis and guard cell metabolism impacts on stomatal behavior. New Phytol **203**: 1064–1081

Lawson T, Vialet-Chabrand S (2019) Speedy stomata, photosynthesis and plant water use efficiency. New Phytol **221**: 93–98

Laza MaRC, Kondo M, Ideta O, Barlaan E, Imbe T (2010) Quantitative trait loci for stomatal density and size in lowland rice. Euphytica **172**: 149–158

Leakey ADB, Ferguson JN, Pignon CP, Wu A, Jin Z, Hammer GL, Lobell DB (2019) Water use efficiency as a constraint and target for improving the resilience and productivity of C3 and C4 crops. Annu Rev Plant Biol **70**: 781–808

Li K, Huang J, Song W, Wang J, Lv S, Wang X (2019) Automatic segmentation and measurement methods of living stomata of plants based on the CV model. Plant Methods **15**: 67

Liao J-X, Chang J, Wang G-X (2005) Stomatal density and gas exchange in six wheat cultivars. Cereal Res Commun **33**: 719–726

Lin T-YY, Zitnick CL, Doll P, Maire M, Belongie S, Hays J, Perona P, Ramanan D, Dollár P, Zitnick CL, et al. (2014) Microsoft COCO: common objects in context. *In* Lecture Notes in Computer Science (including subseries Lecture Notes in Artificial Intelligence and Lecture Notes in Bioinformatics). doi: 10.1007/978-3-319-10602-1_48

Liu X, Mak M, Babla M, Wang F, Chen G, Veljanoski F, Wang G, Shabala S, Zhou M, Chen ZH (2014) Linking stomatal traits and expression of slow anion channel genes HvSLAH1 and HvSLAC1 with grain yield for increasing salinity tolerance in barley. Front Plant Sci **5**: 634

Liu X, Fan Y, Mak M, Babla M, Holford P, Wang F, Chen G, Scott G, Wang G, Shabala S et al. (2017) QTLs for stomatal and photosynthetic traits related to salinity tolerance in barley. BMC Genomics **18**: 9

Liu S, Tang J, Petrie P, Whitty M (2016) A Fast Method to Measure Stomatal Aperture by MSER on Smart Mobile Phone. p AIW2B.2

Lobell DB, Roberts MJ, Schlenker W, Braun N, Little BB, Rejesus RM, Hammer GL (2014) Greater sensitivity to drought accompanies maize yield increase in the U.S. Midwest. Science **344**: 516–519

Markelz RJC, Strellner RS, Leakey ADB (2011) Impairment of C4 photosynthesis by drought is exacerbated by limiting nitrogen and ameliorated by elevated [CO_2] in maize. J Exp Bot **62**: 3235–3246.

McAusland L, Vialet-Chabrand S, Davey P, Baker NR, Brendel O, Lawson T (2016) Effects of kinetics of light-induced stomatal responses on photosynthesis and water-use efficiency. New Phytol **211**: 1209–1220

McKown KH, Bergmann DC (2020) Stomatal development in the grasses: lessons from models and crops (and crop models). New Phytol **227**: 1587–1590. nph.16450

McMullen MD, Kresovich S, Villeda HS, Bradbury P, Li H, Sun Q, Flint-Garcia S, Thornsberry J, Acharya C, Bottoms C, et al. (2009) Genetic properties of the maize nested association mapping population. Science **325**: 737–740

Miskin KE, Rasmusson DC, Moss DN (1972) Inheritance and physiological effects of stomatal frequency in barley. Crop Sci **12**: 780–783. cropsci1972.0011183X001200060019x

Mochida K, Koda S, Inoue K, Nishii R (2018) Statistical and machine learning approaches to predict gene regulatory networks from transcriptome datasets. Front Plant Sci **9**: 1770. doi: 10.3389/fpls.2018.01770

Muchow RC, Sinclair TR (1989) Epidermal conductance, stomatal density and stomatal size among genotypes of Sorghum bicolor (L.) Moench. Plant Cell Environ **12**: 425–431

Ohsumi A, Kanemura T, Homma K, Horie T, Shiraiwa T (2007) Genotypic variation of stomatal conductance in relation to stomatal density and length in rice (Oryza sativa L.). Plant Prod Sci **10**: 322–328

Omasa K, Onoe M (1984) Measurement of stomatal aperture by digital image processing. Plant Cell Physiol **25**: 1379–1388. doi: 10.1093/oxfordjournals.pcp.a076848

Panda D, Mahakhud A, Mohanty B, Mishra SS, Barik J (2018) Genotypic variation of photosynthetic gas exchange and stomatal traits in some traditional rice (Oryza sativa L.) landraces from Koraput, India for crop improvement. Physiol Mol Biol Plants **24**: 973–983

Patto MCV, Rubiales D, Martín A, Hernμndez P, Lindhout P, Niks R E, Stam P (2003) QTL mapping provides evidence for lack of association of the avoidance of leaf rust in Hordeum chilense with stomata density. Theor Appl Genet **106**: 1283–1292

Pelleschi S, Leonardi A, Rocher J-P, Cornic G, de Vienne D, Thévenot C, Prioul J-L (2006) Analysis of the relationships between growth, photosynthesis and carbohydrate metabolism using quantitative trait loci (QTLs) in young maize plants subjected to water deprivation. Mol Breed **17**: 21–39

Pignon CP, Leakey ADB, Long SP, Kromdijk J (2021) Drivers of natural variation in water-use efficiency under fluctuating light are promising targets for improvement in sorghum. Front Plant Sci **12**: 627432. doi: 10.3389/fpls.2021.627432

Pillitteri LJ, Torii KU (2012) Mechanisms of stomatal development. Annu Rev Plant Biol **63**: 591–614.

Prakash PT, Banan D, Paul RE, Feldman MJ, Xie D, Freyfogle L, Baxter I, Leakey ADB (2020) Correlation and co-localization of QTL for stomatal density and canopy temperature under drought stress in Setaria. J Exp Bot **72**: 5024–5037

Qu X, Yan M, Zou J, Jiang M, Yang K, Le J (2018) A2-type cyclin is required for the asymmetric entry division in rice stomatal development. J Exp Bot **69**: 3587–3599

Raissig MT, Abrash E, Bettadapur A, Vogel JP, Bergmann DC (2016) Grasses use an alternatively wired bHLH transcription factor network to establish stomatal identity. Proc Natl Acad Sci U S A **113**: 8326–8331

Raissig MT, Matos JL, Gil MXA, Kornfeld A, Bettadapur A, Abrash E, Allison HR, Badgley G, Vogel JP, Berry JA, et al. (2017) Mobile MUTE specifies subsidiary cells to build physiologically improved grass stomata. Science **355**: 1215–1218

Royer DL (2001) Stomatal density and stomatal index as indicators of paleoatmospheric CO_2 concentration. Rev Paleobot Palynol **114**: 1–28.

Sack L, Cowan PD, Jaikumar N, Holbrook NM (2003) The "hydrology" of leaves: co-ordination of structure and function in temperate woody species. Plant Cell Environ **26**: 1343–1356

Sakoda K, Watanabe T, Sukemura S, Kobayashi S, Nagasaki Y, Tanaka Y, Shiraiwa T (2019) Genetic diversity in stomatal density among soybeans elucidated using high-throughput technique based on an algorithm for object detection. Sci Rep **9**: 7610

Saponaro P, Treible W, Kolagunda A, Chaya T, Caplan J, Kambhamettu C, Wisser R (2017) DeepXScope: segmenting microscopy images with a deep neural network. *In* IEEE Computer Society Conference on Computer Vision and Pattern Recognition Workshops, July 2017. pp 843–850

Schneider CA, Rasband WS, Eliceiri KW (2012) NIH Image to ImageJ: 25 years of image analysis. Nat Methods **9**: 671–675. doi: 10.1038/nmeth.2089

Schoppach R, Taylor JD, Majerus E, Claverie E, Baumann U, Suchecki R, Fleury D, Sadok W (2016) High resolution mapping of traits related to whole-plant transpiration under increasing evaporative demand in wheat. J Exp Bot **67**: 2847–2860

Schroeder JI, Allen GJ, Hugouvieux V, Kwak JM, Waner D (2001) Guard cell signal transduction. Annu Rev Plant Physiol Plant Mol Biol **52**: 627–658

Shahinnia F, Le Roy J, Laborde B, Sznajder B, Kalambettu P, Mahjourimajd S, Tilbrook J, Fleury D (2016) Genetic association of stomatal traits and yield in wheat grown in low rainfall environments. BMC Plant Biol **16**: 150

Singh AK, Ganapathysubramanian B, Sarkar S, Singh A (2018) Deep learning for plant stress phenotyping: trends and future perspectives. Trends Plant Sci **23**: 883–898

Sumathi M, Bachpai VKW, Deeparaj B, Mayavel A, Dasgupta G, Nagarajan B, Rajasugunasekar D, Sivakumar V, Yasodha R (2018) Quantitative trait loci mapping for stomatal traits in interspecific hybrids of Eucalyptus. J Genet **97**: 323–329

Taylor SH, Franks PJ, Hulme SP, Spriggs E, Christin PA, Edwards EJ, Woodward FI, Osborne CP (2012) Photosynthetic pathway and ecological adaptation explain stomatal trait diversity amongst grasses. New Phytol **193**: 387–396

Taylor SH, Lowry DB, Aspinwall MJ, Bonnette JE, Fay PA, Juenger TE (2016) QTL and Drought Effects on Leaf Physiology in Lowland Panicum virgatum. Bioenerg Res **9**: 1241–1259

Teng S, Qian Q, Zeng D, Kunihiro Y, Fujimoto K, Huang D, Zhu L (2004) QTL analysis of leaf photosynthetic rate and related physiological traits in rice (Oryza sativa L.). Euphytica **135**: 1–7

Toda Y, Toh S, Bourdais G, Robatzek S, Maclean D, Kinoshita T (2018) DeepStomata: facial recognition technology for automated stomatal aperture measurement. bioRxiv https://doi.org/10.1101/365098

Torii KU (2015) Stomatal differentiation: the beginning and the end. Curr Opin Plant Biol **28**: 16–22

Ubbens JR, Stavness I (2017) Deep plant phenomics: a deep learning platform for complex plant phenotyping tasks. Front Plant Sci **8**: 1190. doi: 10.3389/fpls.2017.01190

USDA (2019) World Agricultural Supply and Demand Estimates (WASDE). https://www.usda.gov/oce/commodity/wasde/ (July, 2020)

USDA (2020) Foreign Agricultural Service. https://www.fas.usda.gov/data/grain-world-markets-and-trade

Vanneste S, Coppens F, Lee E, Donner TJ, Xie Z, Van Isterdael G, Dhondt S, De Winter F, De Rybel B, Vuylsteke M, et al. (2011) Developmental regulation of CYCA2s contributes to tissue-specific proliferation in Arabidopsis. EMBO J **30**: 3430–3441

Vialet-Chabrand S, Brendel O (2014) Automatic measurement of stomatal density from microphotographs. Trees **28**: 1859–1865

Vőfély RV, Gallagher J, Pisano GD, Bartlett M, Braybrook SA (2019) Of puzzles and pavements: a quantitative exploration of leaf epidermal cell shape. New Phytol **221**: 540–552

Wu Z, Chen L, Yu Q, Zhou W, Gou X, Li J, Hou S (2019) Multiple transcriptional factors control stomata development in rice. New Phytol **223**: 220–232

Yasir TA, Min D, Chen X, Condon AG, Hu Y-G (2013) The association of carbon isotope discrimination (Δ) with gas exchange parameters and yield traits in Chinese bread wheat cultivars under two water regimes. Agric Water Manag **119**: 111–120

Yin X, Biswal AK, Dionora J, Perdigon KM, Balahadia CP, Mazumdar S, Chater C, Lin H-C, Coe RA, Kretzschmar T, et al. (2017) CRISPR-Cas9 and CRISPR-Cpf1 mediated targeting of a stomatal developmental gene EPFL9 in rice. Plant Cell Rep **36**: 745–757

Yoo CY, Pence HE, Jin JB, Miura K, Gosney MJ, Hasegawa PM, Mickelbart MV (2010) The Arabidopsis GTL1 transcription factor regulates water use efficiency and drought tolerance by modulating stomatal density via transrepression of SDD1. Plant Cell **22**: 4128–4141

Yu J, Holland JB, McMullen MD, Buckler ES (2008) Genetic design and statistical power of nested association mapping in maize. Genetics **178**: 539–551

Waleed A (2017) GitHub – matterport/Mask_RCNN: Mask R-CNN for Object Detection and Instance Segmentation on Keras and TensorFlow. https://github.com/matterport/Mask_RCNN

Wolz KJ, Wertin TM, Abordo M, Wang D, Leakey ADB (2017) Variation in stomatal function is integral to modeling plant carbon and water fluxes. Nat Ecol Evol **1**:1292–1298